A&A, 711, A12 (2026)
https://doi.org/10.1051/0004-6361/202557633
© The Authors 2026

Astronomy & Astrophysics
Special issue

Euclid Quick Data Release (Q1)

Euclid Quick Data Release (Q1)

XII. Quenching precedes bulge formation in dense environments but follows it in the field

Euclid Collaboration: F. Gentile[1,2,⋆], E. Daddi[3], D. Elbaz[3], A. Enia[4,2], B. Magnelli[3], J.-B. Billand[1], P. Corcho-Caballero[5], C. Cleland[6], G. De Lucia[7], C. D'Eugenio[8,1], M. Fossati[9,10], M. Franco[3], C. Lobo[11,12], Y. Lyu[1], M. Magliocchetti[13], G. A. Mamon[14,15], L. Quilley[16], J. G. Sorce[17,18], M. Tarrasse[1], M. Bolzonella[2], F. Durret[15], L. Gabarra[19], S. Guo[1], L. Pozzetti[2], S. Quai[20,2], F. Shankar[21], V. Sangalli[1,3], M. Talia[20,2], M. Baes[22], H. Fu[23,21], M. Girardi[24,7], J. Matthee[25], P. A. Oesch[26,27,28], D. Roberts[21], J. Schaye[29], D. Scott[30], L. Spinoglio[13], B. Altieri[31], A. Amara[32], S. Andreon[10], N. Auricchio[2], C. Baccigalupi[33,7,34,35], M. Baldi[4,2,36], A. Balestra[37], S. Bardelli[2], R. Bender[38,39], A. Biviano[7,33], E. Branchini[40,41,10], M. Brescia[42,43], J. Brinchmann[11,44,45], S. Camera[46,47,48], G. Cañas-Herrera[49,29], V. Capobianco[48], C. Carbone[50], J. Carretero[51,52], S. Casas[53,54], M. Castellano[55], G. Castignani[2], S. Cavuoti[43,56], K. C. Chambers[57], A. Cimatti[58], C. Colodro-Conde[59], G. Congedo[60], L. Conversi[61,31], Y. Copin[62], F. Courbin[63,64], H. M. Courtois[65], M. Cropper[66], A. Da Silva[67,68], H. Degaudenzi[26], C. Dolding[66], H. Dole[18], F. Dubath[26], C. A. J. Duncan[60], X. Dupac[31], S. Dusini[69], S. Escoffier[70], M. Fabricius[38,39], M. Farina[13], R. Farinelli[2], S. Ferriol[62], F. Finelli[2,71], N. Fourmanoit[70], M. Frailis[7], E. Franceschi[2], M. Fumana[50], S. Galeotta[7], K. George[72], B. Gillis[60], C. Giocoli[2,36], J. Gracia-Carpio[38], A. Grazian[37], F. Grupp[38,39], S. Gwyn[73], S. V. H. Haugan[74], J. Hoar[31], W. Holmes[75], I. M. Hook[76], F. Hormuth[77], A. Hornstrup[78,79], K. Jahnke[80], M. Jhabvala[81], B. Joachimi[82], E. Keihänen[83], S. Kermiche[70], A. Kiessling[75], B. Kubik[62], M. Kümmel[39], M. Kunz[84], H. Kurki-Suonio[85,86], A. M. C. Le Brun[87], S. Ligori[48], P. B. Lilje[74], V. Lindholm[85,86], I. Lloro[88], G. Mainetti[89], D. Maino[90,50,91], E. Maiorano[2], O. Mansutti[7], O. Marggraf[92], M. Martinelli[55,93], N. Martinet[94], F. Marulli[20,2,36], R. J. Massey[95], E. Medinaceli[2], S. Mei[6,96], M. Melchior[97], Y. Mellier[15,14,†], M. Meneghetti[2,36], E. Merlin[55], G. Meylan[98], A. Mora[99], M. Moresco[20,2], L. Moscardini[20,2,36], R. Nakajima[92], S.-M. Niemi[49], C. Padilla[100], S. Paltani[26], F. Pasian[7], K. Pedersen[101], W. J. Percival[102,103,104], V. Pettorino[49], S. Pires[3], G. Polenta[105], M. Poncet[106], L. A. Popa[107], F. Raison[38], A. Renzi[108,69], J. Rhodes[75], G. Riccio[43], E. Romelli[7], M. Roncarelli[2], R. Saglia[39,38], Z. Sakr[109,110,111], D. Sapone[112], B. Sartoris[39,7], P. Schneider[92], T. Schrabback[113], A. Secroun[70], G. Seidel[80], S. Serrano[114,115,116], P. Simon[92], C. Sirignano[108,69], G. Sirri[36], J. Skottfelt[117], L. Stanco[69], J. Steinwagner[38], P. Tallada-Crespí[51,52], A. N. Taylor[60], H. I. Teplitz[118], I. Tereno[67,119], N. Tessore[82], S. Toft[27,28], R. Toledo-Moreo[120], F. Torradeflot[52,51], I. Tutusaus[116,114,110], L. Valenziano[2,71], J. Valiviita[85,86], T. Vassallo[7,72], G. Verdoes Kleijn[5], A. Veropalumbo[10,41,40], Y. Wang[118], J. Weller[39,38], A. Zacchei[7,33], G. Zamorani[2], I. A. Zinchenko[121], E. Zucca[2], V. Allevato[43], M. Ballardini[122,123,2], E. Bozzo[26], C. Burigana[124,71], R. Cabanac[110], M. Calabrese[125,50], A. Cappi[2,126], D. Di Ferdinando[36], J. A. Escartin Vigo[38], W. G. Hartley[26], M. Huertas-Company[59,127,128,129], J. Martín-Fleitas[130], S. Matthew[60], N. Mauri[58,36], R. B. Metcalf[20,2], A. Pezzotta[10], M. Pöntinen[85], I. Risso[10,41], V. Scottez[15,131], M. Sereno[2,36], M. Tenti[36], M. Viel[33,7,35,34,132], M. Wiesmann[74], Y. Akrami[133,134], I. T. Andika[135,136], S. Anselmi[69,108,137], M. Archidiacono[90,91], F. Atrio-Barandela[138], D. Bertacca[108,37,69], M. Bethermin[139], L. Bisigello[37], A. Blanchard[110], L. Blot[140,87], H. Böhringer[38,141,142], M. Bonici[102,50], S. Borgani[24,33,7,34,132], M. L. Brown[143], S. Bruton[144], A. Calabro[55], B. Camacho Quevedo[33,35,7], F. Caro[55], C. S. Carvalho[119], T. Castro[7,34,33,132], F. Cogato[20,2], S. Conseil[62], T. Contini[110], A. R. Cooray[145], O. Cucciati[2], G. Desprez[5], A. Díaz-Sánchez[146], S. Di Domizio[40,41], J. M. Diego[147], P. Dimauro[148,55], P.-A. Duc[139], M. Y. Elkhashab[7,34,24,33], Y. Fang[39], A. Finoguenov[85], A. Fontana[55], F. Fontanot[7,33], A. Franco[149,150,151],

⋆ Corresponding author: fabrizio.gentile@cea.fr
† Deceased.

Open Access article, published by EDP Sciences, under the terms of the Creative Commons Attribution License (https://creativecommons.org/licenses/by/4.0), which permits unrestricted use, distribution, and reproduction in any medium, provided the original work is properly cited.
This article is published in open access under the Subscribe to Open model. Subscribe to A&A to support open access publication.

K. Ganga[6], J. García-Bellido[133], T. Gasparetto[55], V. Gautard[1], R. Gavazzi[94,14], E. Gaztanaga[116,114,152], F. Giacomini[36], F. Gianotti[2], A. H. Gonzalez[153], G. Gozaliasl[154,85], M. Guidi[4,2], C. M. Gutierrez[155,156], A. Hall[60], S. Hemmati[157], H. Hildebrandt[158], J. Hjorth[101], J. J. E. Kajava[159,160], Y. Kang[26], V. Kansal[161,162], D. Karagiannis[122,163], K. Kiiveri[83], J. Kim[19], C. C. Kirkpatrick[83], S. Kruk[31], L. Legrand[164,165], M. Lembo[14,122,123], F. Lepori[166], G. Leroy[167,95], G. F. Lesci[20,2], J. Lesgourgues[53], L. Leuzzi[2], T. I. Liaudat[168], A. Loureiro[169,170], J. Macias-Perez[171], E. A. Magnier[57], F. Mannucci[172], R. Maoli[173,55], C. J. A. P. Martins[174,11], L. Maurin[18], M. Miluzio[31,175], P. Monaco[24,7,34,33,132], C. Moretti[7,33,34,35], G. Morgante[2], K. Naidoo[152,82], A. Navarro-Alsina[92], S. Nesseris[133], D. Paoletti[2,71], F. Passalacqua[108,69], K. Paterson[80], L. Patrizii[36], A. Pisani[70], D. Potter[166], M. Radovich[37], G. Rodighiero[108,37], S. Sacquegna[176,150,149], M. Sahlén[177], D. B. Sanders[57], E. Sarpa[35,132,34], C. Scarlata[178], A. Schneider[166], M. Schultheis[126], D. Sciotti[55,93], E. Sellentin[179,29], L. C. Smith[180], S. A. Stanford[181], K. Tanidis[19], G. Testera[41], R. Teyssier[182], S. Tosi[40,41,10], A. Troja[108,69], M. Tucci[26], C. Valieri[36], A. Venhola[183], D. Vergani[2], G. Verza[184], P. Vielzeuf[70], and N. A. Walton[180]

(Affiliations can be found after the references)

Received 10 October 2025 / Accepted 12 January 2026

ABSTRACT

The well-known bimodality between star-forming discs and quiescent spheroids requires the existence of two main processes: galaxy quenching, causing the strong reduction of star formation, and morphological transformation, causing the transition from disc-dominated structures to bulge-dominated ones. In this paper, we aim to understand the link between these two processes and their relation with the stellar mass of galaxies and their local environment. Taking advantage of the first data released by the Euclid Collaboration, covering more than 60 deg^2 with space-based imaging and photometry, we analyse a mass-complete sample of nearly one million galaxies in the range $0.25 < z < 1$ with $M_* > 10^{9.5}\,M_\odot$, using a combination of photometric and spectroscopic redshifts. We divide the sample into four sub-populations of galaxies, based on their star-formation activity (star-forming and quiescent) and morphology (disc-dominated and bulge-dominated). We then analyse the physical properties of these populations and their relative abundances in the stellar mass versus local density plane. Together with confirming the passivity-density relation and the morphology-density relation, we find that quiescent discy galaxies are more abundant in the low-mass regime of high-density environment where $\log_{10}(1+\delta) > 1.3$. At the same time, star-forming bulge-dominated galaxies are more common in field regions with $\log_{10}(1+\delta) < 0.8$, preferentially at high masses. Building on these results and interpreting them through comparison with simulations, we propose a scenario where the evolution of galaxies in the field significantly differs from that in higher-density environments. The morphological transformation in the majority of field galaxies takes place before the onset of quenching and is mainly driven by secular processes taking place within the main sequence, leading to the formation of star-forming bulge-dominated galaxies as intermediate-stage galaxies. Conversely, quenching of star formation precedes morphological transformation for most galaxies in higher-density environments. This causes the formation of quiescent disc-dominated galaxies before their transition into bulge-dominated ones.

Key words. galaxies: evolution – galaxies: interactions – galaxies: statistics

1. Introduction

When dealing with galaxies, form and substance are tightly connected. Since the introduction of the Hubble sequence (Hubble 1926), it has been well known that the morphology of galaxies strongly correlates with their physical properties (e.g. mass and star-formation rate, SFR; see e.g. Kauffmann et al. 2003; Brinchmann et al. 2004; Wuyts et al. 2011; Huertas-Company et al. 2024). Throughout most of cosmic history (up to at least $z \sim 3$; see e.g. Huertas-Company et al. 2025), this correlation is clearly visible in the bimodal distribution of galaxies, where most of the objects belong to two main families. The first one is characterised by blue rest-frame colours, active star formation, young stellar ages, and discy morphologies. The second one, on the contrary, includes galaxies with redder colours, negligible star formation, older stellar populations, and spheroidal morphologies (see e.g. Strateva et al. 2001; Allen et al. 2006; Euclid Collaboration: Quilley et al. 2026). The limited number of galaxies found in between these populations (see some examples of passive discy galaxies in e.g. Masters et al. 2010 and of star-forming spheroids in e.g. McIntosh et al. 2014) is normally explained through the rapid evolution from one group to another. This process must include both galaxy quenching (i.e. the stopping of star formation; see e.g. Man & Belli 2018 and references therein) and morphological transformation (i.e. the transition from a disc-dominated structure to a bulge-dominated one; see e.g. Liu et al. 2019 and references therein). However, it is not clear whether these two processes take place at the same time or not and – in this second case – if there is a causal connection between them.

The common treatment of galaxy quenching relies on the distinction between two main families of processes: those related to internal factors and those depending on external ones (see e.g. Peng et al. 2010 and references therein). The internal processes include physical mechanisms, such as feedback from massive stars or supernovae (e.g. Ciotti et al. 1991), as well as active galactic nuclei (AGN; e.g. Bower et al. 2006; Croton et al. 2006). These processes are commonly considered together in the general class of 'mass quenching', since they are mostly responsible for stopping of star formation in massive galaxies, regardless of their environment. The second family, instead, includes processes able to inhibit star formation by preventing the accretion of cold gas from the intergalactic medium (starvation; see e.g. Larson et al. 1980; van den Bosch et al. 2008) or by depleting the gas reservoirs in galaxies (e.g. by tidal stripping or ram-pressure stripping; see e.g. Gunn & Gott 1972; Feldmann et al. 2010; Boselli et al. 2022). All these processes are normally referred to as 'environmental quenching', since they are more effective in high-density environments such as galaxy groups or clusters (Feldmann et al. 2010). One of the main results of the current research in this field is that these two effects are separable (i.e. they act independently of each other) and effective at

least since redshift $z \sim 1$ (Peng et al. 2010). At higher redshifts, the picture becomes less clear, and a consensus in the community is still far from being reached, with several studies presenting different conclusions about the effectiveness of environmental quenching at $z > 1.5$ (see, for instance, Fossati et al. 2017; Foltz et al. 2018; Xu et al. 2025; Pan et al. 2025).

When it comes to morphological transformation and its relationship with mass and environmental quenching, scientific literature becomes less rich[1]. While it is well established that the fraction of early-type galaxies is higher at high masses and in high-density environments (see e.g. Dressler 1980; Dressler et al. 1997; Postman et al. 2005; Euclid Collaboration: Cleland et al. 2025), the physical mechanisms able to produce the morphological transformation are still to be completely understood. A possible solution can reside in galaxy mergers, which are able to dissipate angular momentum and cause the transition from disc-dominated structures to bulge-dominated ones (see e.g. Hopkins et al. 2008; Cox et al. 2008), even though it is still debated if the cessation of star formation induced by mergers is permanent or not (see e.g. Dubois et al. 2016; Athanassoula et al. 2016). An analogous debate is still active on the possible effects of feedback mechanisms on the angular momentum of galaxies, and on the consequent possibility of inducing a morphological transformation (see e.g. Übler et al. 2014; Agertz & Kravtsov 2016; Yang et al. 2024). In addition, the possibility of morphological quenching has been proposed by Martig et al. (2009). In this scenario, the formation of a dominant bulge in star-forming galaxies could help stabilise the disc, preventing further star formation.

A full observational test of these scenarios is quite challenging, since it requires wide sky surveys (to sample different environments with different densities), with good photometric constraints (to properly assess photometric redshifts and physical properties of the observed galaxies), and high-resolution imaging (to accurately constrain the morphology of galaxies). Until now, no survey has met all these criteria. On the one hand, wide ground-based surveys missed the key ingredient of high-resolution imaging, while, on the other, space-based missions (such as the *Hubble* Space Telescope or the *James Webb* Space Telescope) are fundamentally limited by their small fields of view, making it hard to perform large sky surveys (see some noteworthy examples in Scoville et al. 2007; Casey et al. 2023).

The recent launch of the *Euclid* satellite (Laureijs et al. 2011; Euclid Collaboration: Mellier et al. 2025) promises to be a game changer in this field. Several studies based on the first data collected by the telescope already showed how – even only relying on photometric redshifts – these data can be employed to characterise the environment of galaxies (e.g. Euclid Collaboration: Cleland et al. 2025), their position in the cosmic web (e.g. Euclid Collaboration: Laigle et al. 2026) and their physical properties (e.g. Euclid Collaboration: Enia et al. 2026; Euclid Collaboration: Tucci et al. 2026). In this study, we aim to address the scientific issues introduced before by adding morphological information to the classical studies focusing on galaxy quenching as a function of mass and environment. In our approach, we focus on the 'intermediate stages' in the transition between star-forming discs and quiescent spheroids: objects with either discy structures and negligible star formation or with predominant bulges and active star formation.

The paper is structured as follows. In Sect. 2, we introduce the first *Euclid* data used in our analysis. In Sect. 3, we describe the procedure followed to estimate the local environmental density for our galaxies. In Sect. 4, we describe the four sub-populations of galaxies considered in our analysis and compute their relative abundances as a function of stellar mass and local density. The observed properties are then linked to the hosting dark matter halos through comparison with simulations. These observational results are then employed in Sect. 5 to propose an evolutionary scenario for the four sub-populations. Finally, we draw our conclusions in Sect. 6 and present the future perspectives of our work in anticipation of the next data releases from the *Euclid* satellite.

Throughout this paper, we assume a standard ΛCDM cosmology with the parameters reported in Planck Collaboration VI (2020). We also assume a Chabrier (2003) initial mass function. Finally, all the magnitudes quoted throughout the text are reported in the AB photometric system (Oke & Gunn 1983).

2. Data

2.1. The Euclid survey and the Q1 data

During the nominal duration of its mission, the *Euclid* satellite will carry out a wide survey covering almost $14\,000\,\mathrm{deg}^2$ of the extragalactic sky (Euclid Collaboration: Scaramella et al. 2022). As part of this survey, it will collect space-based imaging in one broad visible (VIS) filter (I_E; Euclid Collaboration: Cropper et al. 2025) and three near-infrared (NIR) filters (Y_E, J_E, and H_E; Euclid Collaboration: Jahnke et al. 2025), together with slitless spectroscopy at NIR wavelengths (Euclid Collaboration: Gillard et al. 2026). This wide survey will be complemented by a deeper one (covering the three Euclid Deep Fields – EDFs – for a total of more than $50\,\mathrm{deg}^2$ at the end of the survey) with significantly higher exposure times (expected gain of about two magnitudes in photometry; see Euclid Collaboration: Mellier et al. 2025). We refer to Laureijs et al. (2011) and Euclid Collaboration: Mellier et al. (2025) for a complete description of the *Euclid* satellite, its main scientific goals, and the technical details of the telescope.

In this paper, we analyse the first data released by the Euclid Consortium (the Euclid Quick Release Q1 2025; Q1 in the following, see Euclid Collaboration: Aussel et al. 2026). These data cover $63.1\,\mathrm{deg}^2$, divided between the deep fields Fornax (EDF-F; $12.1\,\mathrm{deg}^2$), North (EDF-N; $22.9\,\mathrm{deg}^2$), and South (EDF-S; $28.1\,\mathrm{deg}^2$). The 10σ depth of the Q1 data (measured in a circular aperture with a radius equal to twice the full width half maximum of the point spread function; PSF FWHM) is fixed to $I_\mathrm{E} = 24.5$, equivalent to the nominal depth of the wide survey at the end of the mission lifetime. A complete description of the Q1 data can be found in Euclid Collaboration: Aussel et al. (2026).

For our analysis, we employ the photometric redshifts and physical properties (stellar masses, SFR[2], and rest-frame colours) estimated in Euclid Collaboration: Enia et al. (2026) through the machine-learning algorithm Nearest-Neighbour Photometric Redshift (`nnpz`; see Euclid Collaboration: Desprez et al. 2020; Euclid Collaboration: Enia et al. 2024). These data differ from the standard data products included in the Q1 release (see their descriptions in Euclid Collaboration: McCracken et al. 2026; Euclid Collaboration: Polenta et al. 2026; Euclid Collaboration: Romelli et al. 2026; Euclid Collaboration: Tucci et al. 2026). We refer to Euclid Collaboration: Enia et al. (2026) for a complete discussion on the main differences between the two data-sets. Here, we highlight the fact that the physi-

[1] It is interesting how taking the morphological transformation into account was already seen as a priority by Peng et al. (2010).

[2] Throughout this study, we use a SFR averaged on the last 100 Myr of the star formation history of each galaxy (see Euclid Collaboration: Tucci et al. 2026; Euclid Collaboration: Enia et al. 2026).

cal properties obtained by Euclid Collaboration: Enia et al. (2026) are computed by taking into account the *Euclid* photometry (I_E, Y_E, J_E, and H_E bands), the external ground-based photometry collected between 0.3 µm and 1.8 µm by the Ultraviolet Near-Infrared Optical Northern Survey (UNIONS; Gwyn et al. 2025) and the Dark Energy Survey (DES; Flaugher et al. 2015; Dark Energy Survey Collaboration 2016), and the mid-infrared (MIR) photometry at 3.6 µm and 4.5 µm collected by *Spitzer*/IRAC and extracted by Euclid Collaboration: Bisigello et al. (2026). The last component is not included in the official data products by the Euclid Collaboration, even though it is available for most of the sources from the Q1 release thanks to the Cosmic Dawn Survey of the Euclid Deep and Auxiliary Fields (DAWN; Euclid Collaboration: Moneti et al. 2022; Euclid Collaboration: McPartland et al. 2025). The inclusion of MIR photometry produces a significant improvement in the accuracy of the photometric redshifts and stellar masses, especially at higher redshifts (see the discussion in Euclid Collaboration: Enia et al. 2026).

The second tier of data products employed in this analysis consists of the morphological parameters estimated by the MERge Processing Function (MER PF; Euclid Collaboration: Romelli et al. 2026). Specifically, we make use of the modelling with a single bi-dimensional Sérsic profile (Sérsic 1963) performed on the VIS images. The modelling is performed with the `SourceXtractor++` code (Bertin et al. 2020; Kümmel et al. 2022), as described in more detail in Euclid Collaboration: Quilley et al. (2026).

2.2. Sample selection

As already done in several studies analysing the first *Euclid* data, we apply a series of criteria to clean the sample from spurious detections. These are based on the quality flags introduced by Euclid Collaboration: Tucci et al. (2026) and correspond to those employed in Euclid Collaboration: Enia et al. (2026):

$$\begin{cases} \texttt{SPURIOUS_FLAG} = 0; \\ \texttt{DET_QUALITY_FLAG} < 4. \end{cases} \tag{1}$$

These criteria are useful to avoid spurious detections and sources that are saturated or too close to the borders of the detection image. In addition to these criteria, we aim to remove as many non-galaxies and point sources as possible from our sample, so we add some extra conditions following Euclid Collaboration: Matamoro Zatarain et al. (2026) and Euclid Collaboration: Quilley et al. (2026):

$$\begin{cases} \texttt{MUMAX_MINUS_MAG} > -2.6; \\ \texttt{PROB_QSO} < 0.86; \\ \texttt{PROB_STAR} < 0.10; \\ q > 0.05; \\ 0.01a < R_e < 2a. \end{cases} \tag{2}$$

Here, q and R_e are the axis ratio and effective radius of the Sérsic profile, a is the major semi-axis of the segmentation area, `MUMAX_MINUS_MAG` is a compactness criterion defined as the difference between the peak surface brightness and the total magnitude in the detection band, and `PROB_QSO` and `PROB_STAR` quantify the probability of a given object to be a quasi-stellar object (QSO) or a star, respectively. As reported in Euclid Collaboration: Tucci et al. (2026), the QSO classification is obtained through a random forest classifier and achieved a 95% success rate when validated on a spectroscopic sample of non-stellar objects. This value increases slightly when the threshold adopted in Equation (2) is chosen, as reported by Euclid Collaboration: Matamoro Zatarain et al. (2026).

Finally, we aim at analysing a complete sample of galaxies in the redshift range $0.25 < z < 1$. Therefore, we choose to work with a flux- and mass-limited sample. For doing so, we perform a last series of cuts:

$$\begin{cases} H_E < 24; \\ M_* > 10^{9.5}\, M_\odot; \\ 0.25 < z_{phot} < 1. \end{cases} \tag{3}$$

The first condition roughly corresponds to a S/N > 5 cut in the H_E band, which allows us to focus on a sample of galaxies with good constraints in the NIR regime. The chosen limiting mass corresponds to the 95% completeness limit for quiescent galaxies with $H_E < 24$ at $z \sim 1$, as estimated by Euclid Collaboration: Enia et al. (2026) following the standard relation of Pozzetti et al. (2010) applied to their data products. Given the overall behaviour of the mass completeness, the percentage is clearly higher at lower redshifts and for star-forming galaxies. The chosen redshift range allows us to focus on galaxies covering a significant cosmological volume and with an accurate photometric redshift (see Sect. 3). The final sample of galaxies employed to estimate the density field (Sect. 3) includes 975 830 objects. The rest of the analysis, where we intensively take advantage of the morphological parameters, is based on a sub-sample of 876 727 galaxies with

$$\begin{cases} q < 1; \\ 0.302 < n_{Ser} < 5.45, \end{cases} \tag{4}$$

where n_{Ser} is the Sérsic index. These cuts are prescribed by Euclid Collaboration: Quilley et al. (2026) to remove from the sample galaxies with inaccurate morphological analysis.

2.3. Ancillary spectroscopy

To incorporate the spectroscopic information available for some of the galaxies observed in Q1, we take advantage of the spectroscopic compilation available within the Euclid Consortium (C. Saulder, private communication). This collection includes redshifts from: the Dark Energy Spectroscopic Instrument (DESI, DESI Collaboration 2016, 2024); the 16th Data Release of the Sloan Digital Sky Survey (SDSS, Ahumada et al. 2020); the 2MASS Redshift Survey (2MRS, Huchra et al. 2012); the PRIsm MUlti-object Survey (PRIMUS, Coil et al. 2011); the Australian Dark Energy Survey (OzDES, Yuan et al. 2015; Childress et al. 2017; Lidman et al. 2020); 3dHST (Brammer et al. 2012); the 2-degree Field Galaxy Redshift Survey (2dFGRS, Colless et al. 2001); the 6-degree Field Galaxy Redshift Survey (6dFGS, Jones et al. 2009); the MOSFIRE Deep Evolution Field Survey (MOSDEF, Kriek et al. 2015); the VANDELS ESO public spectroscopic survey (Pentericci et al. 2018; Talia et al. 2023); the JWST Advanced Deep Extragalactic Survey DR3 (JADES, D'Eugenio et al. 2025); the 2-degree Field Lensing Survey (2dFLens, Blake et al. 2016); and the VIMOS VLT deep survey (VVDS, Le Fèvre et al. 2005). These are all matched to *Euclid* sources. We only include in our procedure sources with secure redshifts (i.e. with quality flag $Q_f \geq 3$), obtaining a spectroscopic coverage of about 5% of the galaxies involved in the analysis, decreasing quite linearly from 10% at $z = 0.25$ to 2% at $z = 1$. In

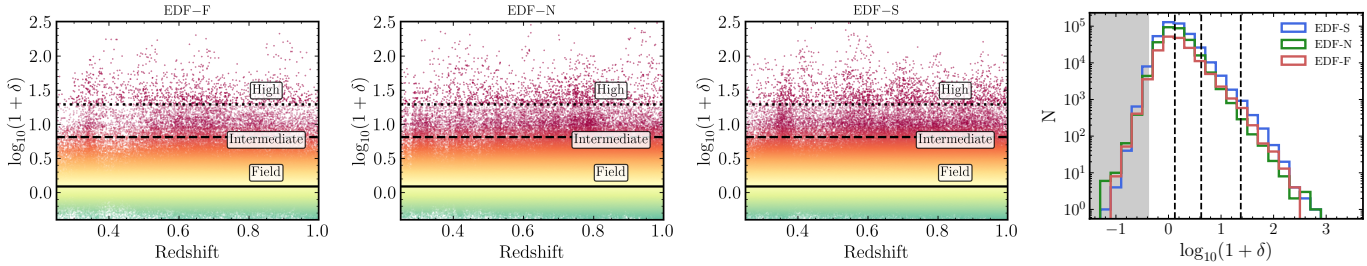


Fig. 1. *First three panels*: Density field as estimated in Sect. 3 for the three EDFs. The three panels show the density contrast parameter as a function of the redshift in each field. The horizontal solid, dashed, and dotted lines represent the median value of $\log_{10}(1+\delta)$, the 2σ, and the 5σ levels, respectively. They separate the field, intermediate-density regions, and high-density ones. *Last panel*: Distribution of the $\log_{10}(1+\delta)$ in the three EDFs. The dashed lines indicate the same levels as in the previous panels. The shaded area reports the area excluded from the analysis.

the considered redshift range, we find an overall good agreement between the photometric and the spectroscopic redshift, with a $\sigma_{\Delta z/(1+z)} \sim 0.3$. We underline, however, that the spectroscopic coverage is biased towards star-forming galaxies, for which the presence of emission lines makes it easier to model the spectroscopic redshift.

3. Estimation of the density field

We reconstruct the density field of the Q1 galaxies following a tomographic approach, necessary because the accuracy of the available photometric redshifts does not allow a 3D modelling ($\sigma_{\Delta z/(1+z)} \sim 0.03$; see e.g. the discussion in Malavasi et al. 2016 on the possibility of reconstructing the density field with such photometric redshifts). Following Euclid Collaboration: Laigle et al. (2026), we divide the redshift range $0.25 < z < 1$ into 20 overlapping redshift slices with a fixed comoving width of $170\,\mathrm{Mpc}\,h^{-1}$. The overlap is constant and fixed to $90\,\mathrm{Mpc}\,h^{-1}$. The choice of a fixed comoving size for the redshift slices will allow us to compare our results in different redshift bins. Moreover, by employing overlapping slices, we reduce the probability of missing significant overdensities because of the slicing. The lower bound of the redshift range is chosen to sample a large enough volume (and, hence, a large enough sample size), while the upper bound is justified by the decreasing accuracy of the photometric redshifts and by the necessity of analysing a mass-complete sample. Moreover, in this redshift range the VIS filter samples a narrow range of rest-frame optical emission, avoiding biases in the determination of the morphologies (see Sect. 4).

In each redshift slice, we reconstruct the density field through the Σ_N estimator (see e.g. Postman et al. 2005; Baldry et al. 2006; Euclid Collaboration: Cleland et al. 2025), defined as

$$\Sigma_N = \frac{N+1}{\pi R_N^2}, \tag{5}$$

where R_N is the projected distance from the considered galaxy to the N-th closest neighbour. Since the density field is mostly traced by massive galaxies (which, being brighter, are also characterised by a more robust photo-z; $\sigma_{\Delta z/(1+z)} = 0.015$), we compute the Σ_N estimator for the galaxies with $M_* > 10^{10.3}\,M_\odot$ (see e.g. Euclid Collaboration: Laigle et al. 2026) and then assign to the less massive galaxies the density field value of the closest massive neighbour. We underline that our sample is mass-complete at all redshifts with this choice (see Sect. 2.2).

To properly take into account the uncertainties on the photometric redshifts, we rely on a Monte Carlo integration. In practice, we perform 10^3 realisations of the density map of each redshift slice in each of the three EDFs covered by Q1. In each iteration, we randomly sample a value from the Gaussianised probability distribution of the photo-zs for each galaxy. For the galaxies for which a spectroscopic redshift is available (see Sect. 2.3), we model the probability distribution as a delta function centred on the spec-z value.

This procedure allows us to estimate the posterior probability distribution of Σ_N for all the galaxies in our sample. In the following, we will assume as the reference value of Σ_N the median value of the posterior distribution and as the related uncertainty half the symmetrised interval between its 84th and 16th percentiles. Moreover, accounting for the evolution of the mean density of the Universe, in the rest of the analysis we will employ the density contrast parameter, defined as

$$\log_{10}(1+\delta) = \log_{10}\left(1 + \frac{\Sigma_N - \bar{\Sigma}_N}{\bar{\Sigma}_N}\right), \tag{6}$$

where $\bar{\Sigma}_N$ is the median density of the galaxy sample in a given redshift slice. To avoid spurious effects due to galaxies close to the edges of the deep fields and of masked regions, we do not take into account any object with a density contrast parameter lower than $\bar{\Sigma}_N - 2\sigma$, with σ being the standard deviation of the distribution estimated through sigma-clipping.

Finally, we perform the procedure discussed above for several values of N, in the range [3, 10]. Since we notice that the widest dynamical range of $\log_{10}(1+\delta)$ is achieved with $N = 5$, in the rest of the analysis we will only focus on Σ_5. An example of the density field as a function of redshift in the three EDFs is reported in Fig. 1. The estimated density field shows a logarithmically Gaussian shape, with median and standard deviation not evolving strongly with redshift or with the position within the EDFs. Therefore, we highlight three different regimes: in the following we will refer to 'field galaxies' as all the sources with a $\log_{10}(1+\delta)$ below median $+ 2\sigma$, galaxies in 'intermediate density regions' where median $+ 2\sigma < \log_{10}(1+\delta) <$ median $+ 5\sigma$, and 'high density' where $\log_{10}(1+\delta) >$ median $+ 5\sigma$. A quantitative assessment of the reliability of these definitions can be found in the Appendix A.

4. Sub-populations of galaxies

4.1. Classification scheme

Our goal is to analyse the interplay between star formation, stellar mass, environment, morphology, and redshift. Clearly, even with the large statistics offered by the Q1 data, it is extremely

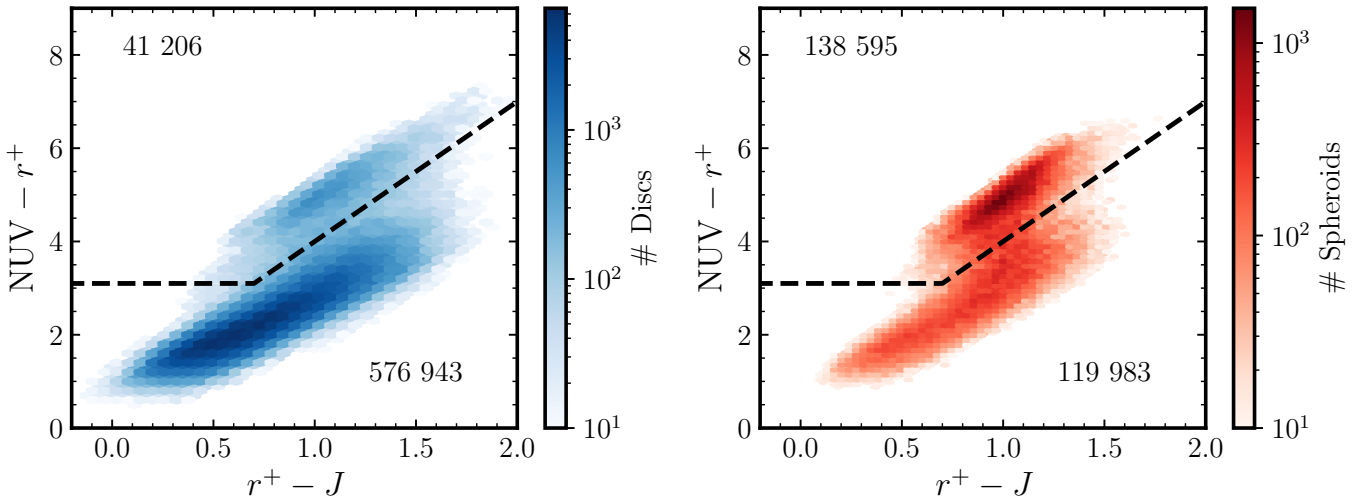


Fig. 2. Selection of star-forming and quiescent galaxies following the rest-frame NUV − r^+ − J colour selection by Ilbert et al. (2010), with the quiescent galaxies located in the upper left part of the plot. The left panel reports the number of discy galaxies belonging to the two selected families, the right panel the number of spheroidal galaxies. The numbers in the two plots report how many galaxies belong to each of the four sub-populations.

challenging to analyse the correlations between so many continuous variables in a multi-dimensional space. For this reason, we simplify the problem by studying the evolution of different sub-populations of galaxies as a function of stellar mass and environment in different redshift bins.

The starting point is the bi-modality reported by Euclid Collaboration: Quilley et al. (2026) in the rest-frame $u-r$ versus Sérsic index plane, which divides the galaxies into red and blue, and into disc-dominated and bulge-dominated[3]. Instead of dividing the sample into the two classical families of early- and late-type galaxies (where the colour information is combined with the morphology), we rely on a classification in four families of objects. The first classification regarding the morphology of galaxies is the same as in Euclid Collaboration: Quilley et al. (2026), employing $n_{\rm Ser} = 2$ as the threshold between disc- and bulge-dominated galaxies.

For the second classification into star-forming and quiescent galaxies, we employ a combination of two rest-frame colours (NUV − r^+ and $r^+ - J$) to have a more robust criterion against contamination by dusty star-forming galaxies than by only using a single $u - r$ colour. We underline that this precaution is needed since the dust content of galaxies is expected to correlate with mass (see e.g. Salim & Narayanan 2020 and references therein), which is one of the variables involved in our analysis. We adopt the selection by Ilbert et al. (2010), classifying as quiescent all the sources with both

$$\begin{cases} \mathrm{NUV} - r^+ > 3(r^+ - J) + 1, \\ \mathrm{NUV} - r^+ > 3.1. \end{cases} \tag{7}$$

We note that this selection is the same employed by Euclid Collaboration: Enia et al. (2026) to compute the mass completeness of the sample; this ensures that our analysis is performed on a 95% mass-complete sample. A visual representation of the selection in Eq. (7) is reported in Fig. 2.

[3] For the sake of brevity, in the following we will refer to these populations as 'discs' and 'spheroids', acknowledging the fact that both components are present in all the objects, with different ratios.

The above-mentioned classifications allow us to separate the full sample of galaxies into four populations. Two of them represent the more common stages of galaxies in the Universe at $z < 1$: the star-forming discs and the quiescent spheroids. These two classes encompass around 82% of the total sample of galaxies at $0.25 < z < 1$ (with 66% of star-forming discs and 16% of quiescent spheroids). The other two classes are normally considered as intermediate phases of the evolution between the two main categories: the quiescent discs and the star-forming spheroids. This intermediate scenario is suggested by their low number densities (∼18% of the total, with 5% of quiescent discs and 13% of star-forming spheroids). Some examples of galaxies belonging to the four families are shown in Fig. 3. We underline that the choice of a single threshold for dividing the two populations is clearly an over-simplification: we expect the population of spheroids to include both objects where the stellar disc is completely absent, as well as others where its contribution is less significant than that of the bulge (e.g. Sa spirals and lenticular galaxies). The proposed classification is affected by two main sources of uncertainty. On the one hand, those coming from the estimation of the physical parameters (i.e. the rest-frame colours) and – consequently – the classification in star-forming and quiescent galaxies. On the other hand, the uncertainty on the Sérsic modelling and the consequent classification in discy and spheroidal galaxies. We explore the effect of these uncertainties on our classification scheme through a Monte Carlo integration, where the four classes are recomputed 10^3 times. For each iteration, a value for the three rest-frame colours and for the Sérsic index is randomly sampled from the Gaussianised posterior probability contained in the catalogues. We report variations of less than 1% in the different classes, ensuring that our classification scheme is robust against the considered uncertainties.

4.2. Population-level properties

A first characterisation of the four sub-populations of galaxies relies on their physical properties. In Fig. 4, we report the relative abundances of the four classes in the stellar mass versus star-formation rate plane in three redshift bins: [0.25, 0.5], [0.5, 0.75], and [0.75, 1.0]. Each pixel reports the rel-

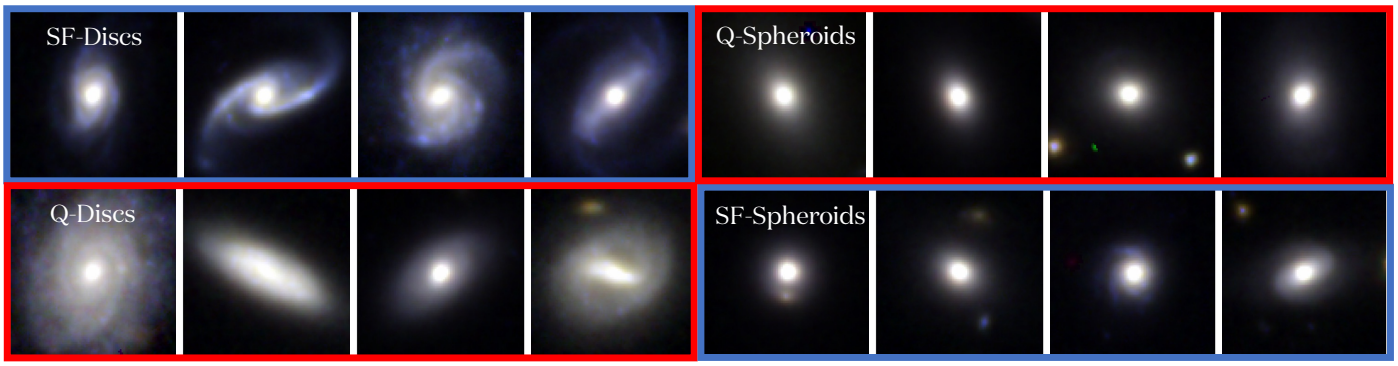


Fig. 3. Some examples of galaxies selected according to the criteria presented in Sect. 4. Starting from the upper left row and proceeding clockwise, the figure shows star-forming discs, quiescent spheroids, star-forming spheroids, and quiescent discs. All the cutouts have a 5 arcsec side and are realised by combining the *Euclid* images in the H_E, Y_E, and I_E filters through the algorithm by Lupton et al. (2004).

ative abundance of one population in the combined bin of redshift, stellar mass, and SFR. The location of the main sequence of star-forming galaxies (MS; see e.g. Elbaz et al. 2011; Schreiber et al. 2015; Popesso et al. 2023) as parametrised by Euclid Collaboration: Enia et al. (2026) by analysing the same data included in this paper is shown for reference.

We find that star-forming discs represent the vast majority of the galaxies in the MS, while the quiescent spheroids populate the so-called red cloud, with SFR at least one dex lower than MS galaxies, and with masses above $10^{10.5}\,M_\odot$. Looking at the two intermediate populations, we see that the quiescent discs represent the majority of galaxies located below the main sequence (at the same distance from the relation by Euclid Collaboration: Enia et al. 2026 as the quiescent spheroids) with stellar masses below $10^{10.5}\,M_\odot$[4]. The star-forming spheroids, instead, represent the majority of galaxies located in the so-called 'green valley' (see e.g. Bell et al. 2004; Schawinski et al. 2014) between the main sequence and the red cloud, at stellar masses higher than $10^{10.5}\,M_\odot$. These results confirm the well-known correlation between morphology and location in the stellar mass versus SFR plane (e.g. Wuyts et al. 2011; Huertas-Company et al. 2024), as well as the mass separation between disc-dominated and bulge-dominated galaxies in the red sequence (e.g. Quilley & de Lapparent 2022). Moreover, the same study by Quilley & de Lapparent (2022) found that the green valley is mostly composed of bulge-dominated objects such as Sa spirals and lenticular galaxies, in good agreement with what is reported in Fig. 4. We also find an interesting difference between our results and those reported by Wuyts et al. (2011): at low masses, we report a higher fraction of quiescent discs, More in detail, we report a median Sérsic index lower than 2 (see also Fig. 12 by Euclid Collaboration: Enia et al. 2026), while Wuyts et al. (2011) finds a higher value for the galaxies located below the main sequence at $M_* < 10^{10.5}\,M_\odot$. However, this tension disappears when we only include galaxies located in the field (see the definition in Sect. 3) in our analysis. This result will be explored in more detail in the next section.

[4] A relative majority of low-mass star-forming discs in the highest redshift bin is also visible in Figure 4. However, this feature is likely a spurious effect due to the low photometric S/N of the galaxies in that region of the diagram. Therefore, we do not include this feature among the results discussed in the remainder of the paper.

4.3. Effects of mass and environment

A second characterisation of the four sub-populations relies on their location in the stellar mass versus local density contrast plane, as shown in Fig. 5. These plots are realised by dividing the parameter space into several bins of mass and $\log_{10}(1+\delta)$, with a fixed logarithmic width of 0.175 dex on both axes. Each pixel represents the relative abundance of each population with respect to the total number of galaxies in the combined bin of redshift, stellar mass, and local density contrast. To ensure the representativeness of our results, we only report in Fig. 5 the bins including at least 15 galaxies. To take into account the uncertainties on the stellar masses and on the characterisation of the environment, all the reported plots are obtained through a Monte Carlo integration, where each plot is realised 10^3 times by sampling each time a different value from the Gaussianised posterior distribution of the stellar masses and the density contrast parameter (see Sect. 3). The reported plots are obtained as the median of the different realisations. We only report in the figure the bins where the signal-to-noise ratio (i.e. the median value of the bin divided by the relative uncertainty estimated as the half-symmetrised interval between the 84th and 16th percentile of the posterior distribution) is higher than three. With this choice, we limit the impact of galaxies with poorly constrained local density.

The main observational results of the plots shown in Fig. 5 are the following. Firstly, we confirm the main findings of several studies such as Peng et al. (2010) and Euclid Collaboration: Cleland et al. 2025: star-forming discs represent the vast majority of galaxies at low masses and in low-density environments, while quiescent spheroids dominate the high-mass and high-density regimes. The transition point (i.e. where the star-forming discs become less than 50% of the total number of galaxies) in the field (i.e. where the effect of environmental quenching is negligible) is located around $10^{10.5}\,M_\odot$, and shows a slight increase with increasing redshift. Both results are in good agreement with what was found by Peng et al. (2010) in their analysis of a spectroscopic sample of galaxies in the Sloan Digital Sky Survey and the zCOSMOS survey, ensuring the reliability of our methods. Analogously, the effects of the environment start to become visible in intermediate and high-density environments (i.e. where the density contrast is above 2σ of the density field, see the horizontal lines in Fig. 5). The effect of environmental quenching is visible as oblique transitions instead of vertical ones at intermediate and high densities (i.e. at fixed masses below $10^{10.5}\,M_\odot$ the fraction of quiescent galaxies increases with increasing local den-

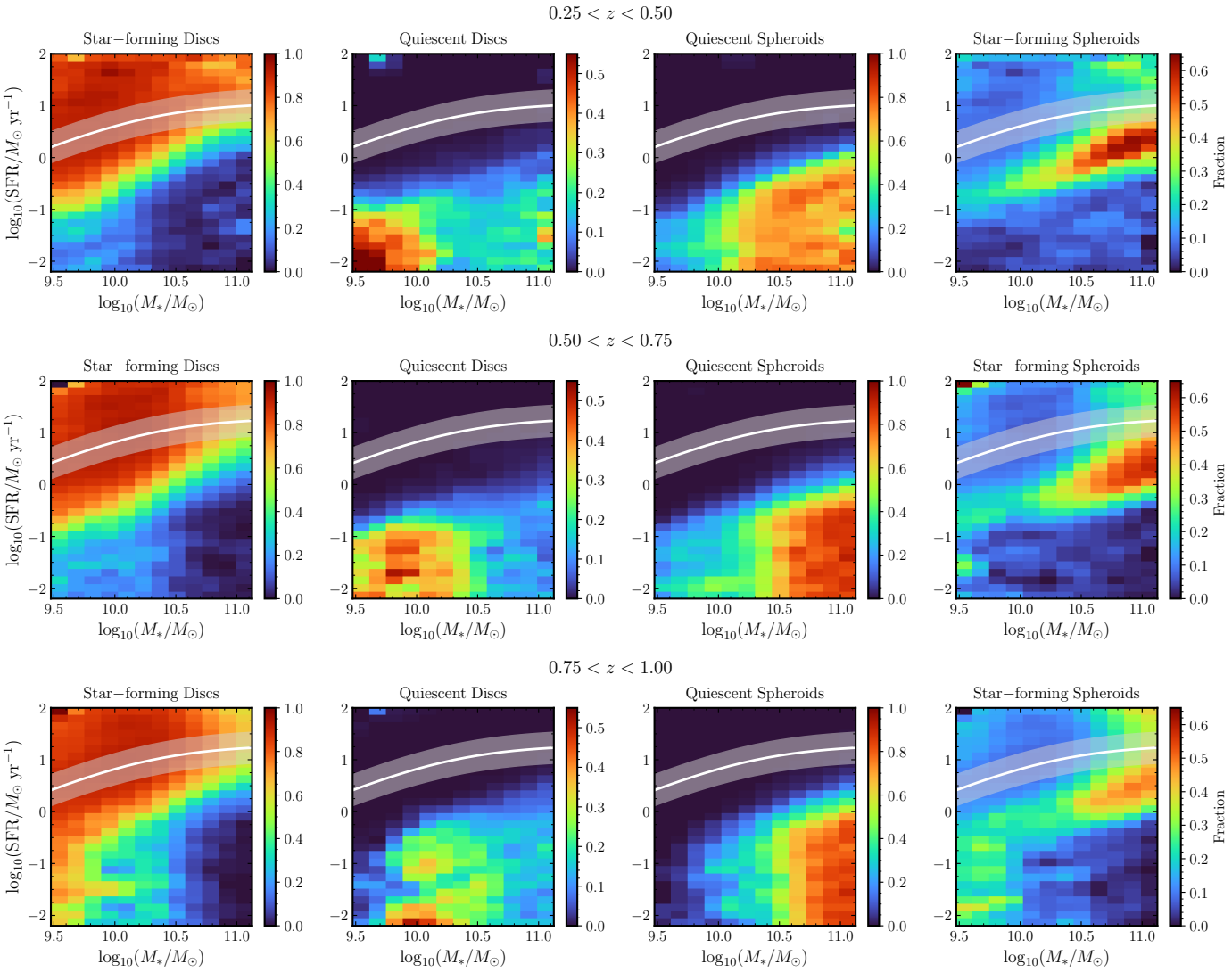


Fig. 4. Four sub-populations of galaxies in the SFR versus stellar mass plane. Each pixel reports the relative abundance of each population through the colour-code reported in the colour-bar (which is different for each panel). The white solid line reports the location of the main sequence of star-forming galaxies as parametrised by Euclid Collaboration: Enia et al. (2026), while the shaded area reports its intrinsic scatter of $\sigma \sim 0.3$ dex.

sity) and also shows an evolution with redshift, with a strength that seems to be much less significant at higher redshift. This result is also in good agreement with what is found by Peng et al. (2010) and Euclid Collaboration: Cleland et al. (2025), suggesting a lower efficiency of environmental quenching at $z > 1$. A possible explanation of this result resides in the evolution of the dynamical state of over-densities with cosmic time (see e.g. Chiang et al. 2017).

Secondly, we observe that quiescent discs represent only a tiny fraction (less than 5%) of the galaxies in the field in the highest redshift bin ($0.75 < z < 1$), with only a slight evolution with cosmic time. Moreover, their relative abundance in the field is found to be independent on the stellar mass[5]. On the other hand, the fraction of these sources is higher in intermediate- and high-density environments, with a strong evolution with cosmic time and with a dependence on stellar mass becoming more evident and complex at lower redshifts. All these findings suggest that the formation of quiescent discs is mainly driven by environmental effects, while their possible transition into quiescent spheroids is mainly due to internal effects, as it will be discussed in detail in Sect. 5.2.

The final observational result concerns the star-forming spheroids. These sources represent a significant fraction (up to 25%) of the galaxies in the high-mass end of the distribution in the field. Their relative abundance in this region of the mass-density plane evolves with cosmic time, decreasing down to less than 20% in the lowest redshift bin ($0.25 < z < 0.5$). On the other hand, these sources are initially (i.e. at $z > 0.75$) found also in over-dense regions (with fractions reaching 20−25%), but then their relative abundance in intermediate- and high-density regions decreases with cosmic time, reaching levels around 10%. These findings suggest that the formation of star-forming spheroids is mainly driven by internal processes and uncommon in over-dense regions, as discussed in greater detail in Sect. 5.1.

4.4. Connection to dark matter halos

To offer a physical interpretation of the observational results presented in Sect. 4.3, we rely on the *Euclid* `Flagship-2` simula-

[5] A small effect is visible in the highest redshift bin, but the overall change in relative abundance is less than 5% and – therefore – not significant in a 95% mass-complete sample, see Sect. 2.

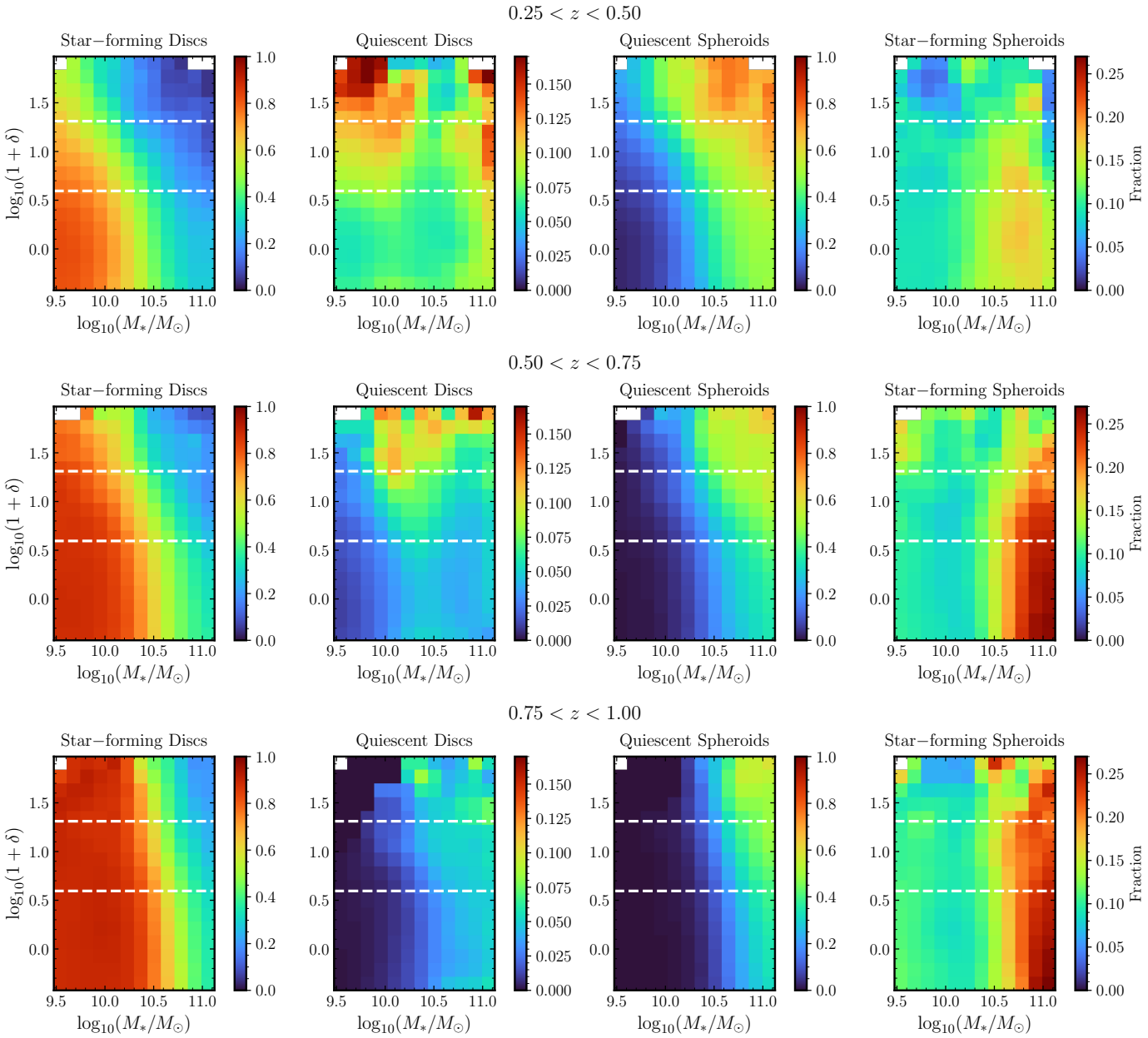


Fig. 5. Relative abundances of the four sub-populations of galaxies analysed in this paper as a function of stellar mass and local density contrast $\log_{10}(1+\delta)$. Each bin has a fixed size of 0.175 dex on both axes. The three rows report the results in three redshift bins with a fixed size of 0.25 in the range $0.25 < z < 1$. The dashed lines separate the different density regions (field, intermediate, and high) defined in Sect. 3 and Fig. 1.

tion (Euclid Collaboration: Castander et al. 2025)[6]. We analyse a light-cone with the same observational properties as the sample introduced so far. In more detail, we focus on an area of 63 deg^2, selecting a mass-limited sample of galaxies following the same criteria introduced in Eq. (3). For these sources, we characterise the environment using the same procedure described in Sect. 3, by employing the same redshift slicing introduced there. Since we are dealing with a simulation, we have access to additional parameters that we could not include in our analysis. Specifically, we have access to the masses of the dark matter halos hosting our sources and to the distinction between central and satellite galaxies (see Euclid Collaboration: Castander et al. 2025). Following the same procedure as in Sect. 4.3, we obtain the plots shown in Fig. 6. There, we report the median halo mass and the fraction of central galaxies as a function of the stellar mass and local density contrast, in the same three redshift bins introduced in the previous sections. Looking at the upper panels of Fig. 6, it is possible to notice how the halo mass tends to increase monotonically with the stellar mass for the galaxies in the field, while it is almost independent on the stellar mass for galaxies in over-dense regions. Moreover, this uniform halo mass for the sources in these latter regions increases with cosmic time (as expected given the evolution of the halo mass function; see e.g. Watson et al. 2013). Looking at the bottom panels of the same figure, we can see how the field is dominated by central galaxies, while the over-dense regions present a clear bi-modality. Specifically, galaxies less massive than $M_* \sim 10^{10.5}\,M_\odot$ are mainly satellites, while the higher masses are dominated by cen-

[6] The `Flagship-2` simulation was retrieved from the CosmoHub portal (Carretero et al. 2017; Tallada et al. 2020): `https://cosmohub.pic.es/home`

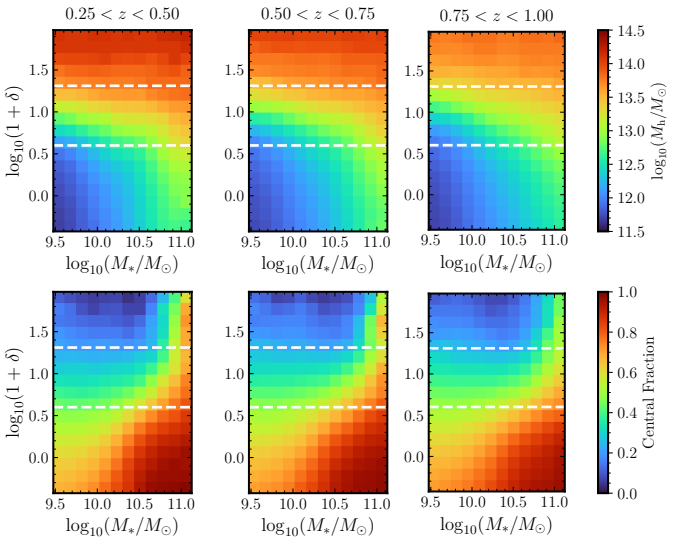


Fig. 6. Median halo mass (*top row*) and fraction of central galaxies (*bottom row*) as a function of stellar mass and local density contrast $\log_{10}(1+\delta)$. The plot is constructed following the same procedure employed for Fig. 5, but analysing the galaxies included in the *Euclid* `Flagship-2` simulation (Euclid Collaboration: Castander et al. 2025). For satellite galaxies, the plot reports the mass of the main dark matter halo. The horizontal dashed lines report the same density regions as in Fig. 1.

tral galaxies. We will use these findings in the next section to develop a physical interpretation of our observational results.

5. Evolutionary implications

In this section, we focus on the possible evolutionary implications of the observational results presented in the previous sections. Based on this evidence, we propose a simple evolutionary scenario where galaxies start their evolution as discs, they evolve as part of the main sequence, then they quench their star formation and reach the red cloud (see also e.g. the analogous studies by Bouché et al. 2010; Wuyts et al. 2011, or Davies et al. 2025). This simple scenario does not include any additional phenomena such as rejuvenation (e.g. Chauke et al. 2019; Mancini et al. 2019; Martín-Navarro et al. 2022) or wet major mergers. The first phenomenon is hard to take into account without proper stellar ages for our objects, but – anyway – it is not expected to impact more than ∼20% of galaxies in the mass and redshift ranges covered by our observations (see e.g. Chauke et al. 2019; Arango-Toro et al. 2025, but also a different perspective by Mancini et al. 2019). Similarly, the impact of wet major mergers on the morphology is expected to be significant only at very high masses ($M_* > 10^{11}\,M_\odot$; see e.g. Rodriguez-Gomez et al. 2017). At the same time, our scenario aims to explain our observations at $z < 1$; therefore it does not account for the possible direct formation of star-forming compact galaxies through – for instance – feedback-free mechanisms (Dekel et al. 2023) expected to take place at higher redshifts.

In our scenario, we will assume that the effects of the environment are negligible in the field (in our analysis, where the density contrast parameter is below $+2\sigma$ from its median value). We acknowledge that this last assumption represents an oversimplification and that a more complete treatment of the problem would require the assembly of a sample of galaxies in cosmic voids (see e.g. Kreckel et al. 2012 and Euclid Collaboration: Papini et al., in prep.).

In this section, we will focus on the formation paths of the two intermediate populations, namely the star-forming spheroids and the quiescent discs as proxies to investigate galaxy quenching and morphological transformation in environments with different densities. A sketch summarising our scenario is shown in Fig. 7.

5.1. Galaxy evolution in the field and role of star-forming spheroids

As noticed in Sect. 4.3, star-forming spheroids represent a significant fraction (up to 25%) of the galaxies at the high-mass end ($M_* > 10^{10.5}\,M_\odot$) in the field, decreasing with cosmic time up to 15% in the lowest redshift bin ($0.25 < z < 0.5$). At the same time, the relative abundance of quiescent spheroids in the field and in the same mass range is found to increase (from ∼30% to ∼50%). We couple these findings with the results presented in Sect. 4.2 and shown in Fig. 4, concerning the abundance of these galaxies in the green valley and at the high-mass end of the main sequence. In addition to these results, we recall that Arango-Toro et al. (2025), in their analysis of the evolutionary path of galaxies in the stellar mass versus SFR plane, found that the vast majority of the galaxies in the green valley were previously located at the high-mass end of the MS (between 70 and 90% at $0.25 < z < 1$) and moves towards the red sequence because of a rapidly declining star-formation activity[7]. All these findings clearly support a scenario where the bulges of star-forming galaxies grow during their evolution as part of the main sequence, together with the growth of stellar mass. Once galaxies reach the high-mass end of the MS, the crossing of the green valley and the transition to the red cloud are driven either by the simple ageing of the stellar population (e.g. Bremer et al. 2018; Phillipps et al. 2019) or by the quenching (either mass- or morphology-driven; e.g. Martig et al. 2009; Peng et al. 2010).

This scenario is supported by several observational results. Firstly, the higher abundance of bulge-dominated galaxies at the high-mass end of the MS and in the green valley (see Fig. 4, but also analogous studies by e.g. Wuyts et al. 2011; Lang et al. 2014; Bremer et al. 2018; Huertas-Company et al. 2024; Euclid Collaboration: Enia et al. 2026; Euclid Collaboration: Quilley et al. 2026). Secondly, the lower abundance of star-forming spheroids in denser environments, decreasing with cosmic time, even in the same mass range where they are more common in the field (see Fig. 5). In this case, most of these sources are the central galaxies of groups (as the vast majority of galaxies with $M_* > 10^{10.5}\,M_\odot$ in dense environment; see Fig. 6, but also analogous studies such as McCracken et al. 2015; Popesso et al. 2019) and – therefore – that the mass quenching efficiency is higher because of the larger halo masses (Sect. 4.4), causing the earlier transition into the class of quiescent spheroids (see e.g. Peng et al. 2012).

In terms of physical processes involved in our scenario for the formation of star-forming spheroids in the field, there is a rich literature of possible mechanisms able to increase the bulge size in star-forming galaxies. The main ones involve the accretion of small satellites via minor mergers (see e.g. Bekki & Couch

[7] We underline, however, that the study by Arango-Toro et al. (2025) is only based on photometric observations. Hence, the reconstruction of non-parametric star formation histories might be affected by biases. Similar studies analysing spectroscopic data (e.g. Mancini et al. 2019) found higher fractions of rejuvenated galaxies in the green valley.

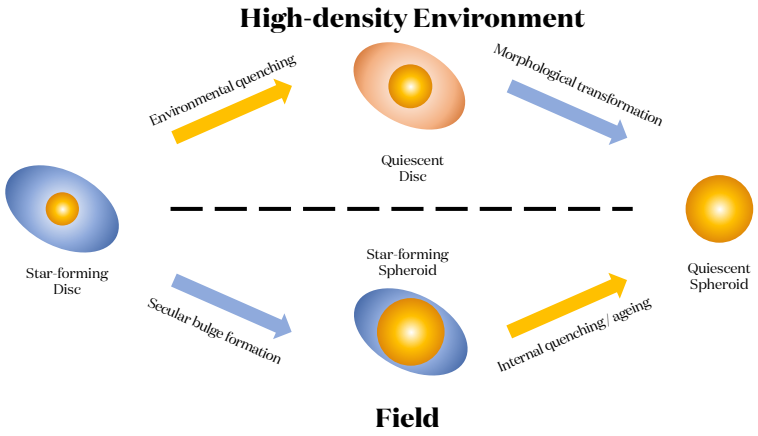


Fig. 7. Sketch summarising the evolutionary scenario inferred from our observational results. The transition from star-forming discs into quiescent spheroids is significantly different in the field and in high-density environments. In the first case, the morphological transformation for most objects happens through secular evolution taking place in the main sequence and it is then followed by quenching by internal processes. In over-dense regions, on the other hand, the quenching for the majority of galaxies is due to external processes and precedes the morphological transformation. Further details in Sect. 5.

2011; Sachdeva et al. 2017; Tacchella et al. 2019), through *in-situ* star formation (see e.g. Noguchi 1999; Dekel et al. 2009a; Yu et al. 2022; Tan et al. 2024; Lyu et al. 2025) potentially resulting from gas accretion with misaligned angular momentum (see e.g. Sales et al. 2012) or clumps formation and migration through disc instabilities (see e.g. Perez et al. 2013; Bournaud 2016). Similarly, the quenching of galaxies in the upper part of the MS can be explained by several mechanisms. A possible cause can reside in the presence of the bulge itself, as in the morphological quenching proposed by Martig et al. (2009), where the bulge causes the stabilisation of the stellar disc and – therefore – the cessation of star formation. An alternative explanation can reside in the accretion of cold gas, expected to be inefficient in massive halos ($M_{\rm h} > 10^{12}\,M_{\odot}$ in the redshift range covered by our observations) due to virial shock heating (see e.g. Birnboim & Dekel 2003; Kereš et al. 2005; Dekel et al. 2009b). This phenomenon can easily explain the decrease of SFR for massive star-forming galaxies (e.g. Daddi et al. 2022). Finally, a role could be played by feedback mechanisms (e.g. by AGN), more common in massive galaxies above $10^{10.5}\,M_{\odot}$ (see e.g. Bongiorno et al. 2016; Chen et al. 2020) and with prominent bulges (e.g. Ferrarese & Merritt 2000; Häring & Rix 2004). A similar scenario would also be in agreement with what has been found by Correa et al. (2019) in their analysis of the EAGLE simulation (Crain et al. 2015; Schaye et al. 2015), where the time of maximum brightness of the SMBH in elliptical galaxies is found to tightly correlate with the time when the same objects cross the green valley, while such a correlation is negligible in discy galaxies.

5.2. Galaxy evolution in high-density environments and role of quiescent discs

In Sect. 4.3, we noticed that the relative abundance of quiescent discs is almost negligible in the field, while it can reach fractions up to 20% in over-dense regions. Moreover, these sources are always located at lower masses with respect to quiescent spheroids in dense environments, in a mass regime where we expect to be dominated by satellite galaxies (see Sect. 4.4 and Fig. 6). At the same time, no significant trend with mass is visible in the field. Finally, their overall abundance increases with decreasing redshift (analogously to the strength of environmental effects).

We interpret all these results as evidence that quiescent discs are formed from star-forming discs through satellite quenching in dense environments. If some of them then stop their evolution, becoming the passive discs observed in the local Universe (e.g. Masters et al. 2010), others keep evolving transitioning into the class of quiescent spheroids. In more detail, in our scenario quiescent discs are prevented from forming stars because of external mechanisms in high-density environments (e.g. through tidal stripping or starvation, depending on the nature and state of the over-density; see e.g. Merritt 1983; Read et al. 2006; Feldmann et al. 2010), lowering the amount of molecular gas available for star formation. Subsequently, other phenomena such as galaxy harassment and minor mergers causes the morphological transformation into bulge-dominated galaxies, eventually increasing their stellar mass. Again, this scenario is in agreement with what has been found by Correa et al. (2019) in the EAGLE simulations, where quiescent discs are mainly found as satellites of groups and clusters and their morphology is transformed after the quenching of their star formation.

6. Summary

In this paper, we characterised the galaxy quenching and the morphological transformation of disc-dominated galaxies into bulge-dominated ones as a function of mass and environment. For our analysis, we took advantage of the first data released by the Euclid Collaboration as part of its Q1 release, which covers about 60 deg^2, reaching a limiting magnitude of $I_{\rm E} = 24.5$. After assembling a mass-complete sample of galaxies with $M_* > 10^{9.5}\,M_{\odot}$ and characterising the density field through the Σ_5 estimator and the corresponding density contrast parameter $\log_{10}(1+\delta)$, we studied the evolution of the relative abundances of four families of galaxies as a function of stellar mass, local density, and redshift. These four classes of galaxies are based on the joint classification between star-forming and quiescent galaxies and disc- and bulge-dominated ones. The unprecedented statistics offered by the *Euclid* telescope allowed us to assemble a statistical significant sample of galaxies belonging to the two intermediate populations of quiescent discs and star-forming spheroids and to study at the same time their distribution in mass and local density field. Our observational results can be summarised as follows.

– Quiescent disc-dominated galaxies represent a negligible fraction of the sources in the field, where their relative abundance does not show any significant correlation with stellar mass. Conversely, these objects are significantly more common in denser environments, where their relative abundance is higher at lower masses and tends to increase with cosmic time.

– Star-forming bulge-dominated galaxies represent a significant fraction of the high-mass galaxies in the field, while their relative abundance at lower masses is negligible in all environments. Moreover, their relative fraction at the high-mass end of high-density environments tends to decrease with cosmic time. Finally, their relative abundance at the high-mass end of the field distribution tends to decrease with cosmic time, while an increasing fraction of quiescent bulge-dominated galaxies appears in the same region of the parameter space.

These findings allow us to propose a simple evolutionary scenario, where the galaxy evolution in the field and in over-dense environments is significantly different. In more detail, our scenario is the following.

– In the field, the morphological transformation of galaxies happens mainly through secular processes taking place as part of the main sequence, with the formation of a dominant bulge once the stellar masses approach $10^{10.5}\,M_{\odot}$, where up to 25% of the galaxies become star-forming bulge-dominated galaxies. The following migration to the red sequence happens thanks to internal processes. These can include the simple ageing of the stellar populations or the quenching, driven by possible mechanisms such as AGN feedback, morphological quenching, or virial shock heating driven by the large halo masses.
– In higher-density environments, the evolution of structures follows the opposite trajectory, with the quenching of star formation taking place before the morphological transformation. In this scenario, the environmental quenching of star-forming discs (mostly satellite galaxies in large dark matter halos) produces quiescent discy galaxies, whose transformation into bulge-dominated quiescent galaxies eventually happens at a following stage through external mechanisms. These can include well-known processes such as dry mergers or galaxy harassment.

These results highlight the scientific potential of the *Euclid* data in constraining the evolution of galaxies in different environments. These results are based on the first quick data release of the Euclid Consortium, covering a small fraction of the total area that will be observed in the wide survey and with a depth up to two magnitudes brighter than what will be reached in the deep survey at the end of the nominal length of the mission. On the one hand, the availability of a wider sky coverage will allow us to cover a larger dynamical range in the density contrast parameter, reaching levels where the environmental quenching is stronger even at higher redshifts. On the other hand, the availability of deeper data will allow us to extend our analysis to lower stellar masses and higher redshifts, to better constrain the photometric redshifts of our sources, and to better characterise their morphologies. In particular, the expected availability of bulge-disc decomposition for the galaxies included in the next data releases will allow us to better discriminate between disc- and bulge-dominated objects. Similarly, the forecasted improvement of the photometric redshifts in the next *Euclid* data releases (see e.g. Euclid Collaboration: Enia et al. 2024), will allow us to reduce the comoving size of our redshift slices and consequently the shot noise affecting the estimation of the density contrast. A final improvement will be represented by the availability of slitless spectroscopy for most of the galaxies observed by *Euclid* (Euclid Collaboration: Le Brun et al. 2026; Euclid Collaboration: Copin et al. 2026). These new data will – on the one hand – increase the spectroscopic coverage of our sample (still limited, see Sect. 2.3), and – on the other hand – allow us to identify remaining AGN. Although we expect our selection criteria, outlined in Section 2, to effectively minimise contamination of our sample by AGN host galaxies, some may still have been included, which potentially affected the physical properties derived by the Euclid pipeline (colours, SFR, and morphology).

Acknowledgements. FaGe, AnEn, EmDa, LoGa, SaQu, GaDe, MaTa, ChDe, LuPo acknowledge support from the ELSA project. "ELSA: Euclid Legacy Science Advanced analysis tools" (Grant Agreement no. 101135203) is funded by the European Union. Views and opinions expressed are however those of the author(s) only and do not necessarily reflect those of the European Union or Innovate UK. Neither the European Union nor the granting authority can be held responsible for them. UK participation is funded through the UK HORIZON guarantee scheme under Innovate UK grant 10093177. AnEn acknowledge support from the INAF MiniGrant 2023 "ADIEU: Anomaly Detections In EUclid". CaLo acknowledges support by FCT-Fundação para a Ciência e a Tecnologia through grants UIDB/04434/2020 DOI: 10.54499/UIDB/04434/2020, UIDP/04434/2020 DOI: 10.54499/UIDP/04434/2020. The Euclid Consortium acknowledges the European Space Agency and a number of agencies and institutes that have supported the development of *Euclid*, in particular the Agenzia Spaziale Italiana, the Austrian Forschungsförderungsgesellschaft funded through BMK, the Belgian Science Policy, the Canadian Euclid Consortium, the Deutsches Zentrum für Luft-und Raumfahrt, the DTU Space and the Niels Bohr Institute in Denmark, the French Centre National d'Etudes Spatiales, the Fundação para a Ciência e a Tecnologia, the Hungarian Academy of Sciences, the Ministerio de Ciencia, Innovación y Universidades, the National Aeronautics and Space Administration, the National Astronomical Observatory of Japan, the Netherlandse Onderzoekschool Voor Astronomie, the Norwegian Space Agency, the Research Council of Finland, the Romanian Space Agency, the State Secretariat for Education, Research, and Innovation (SERI) at the Swiss Space Office (SSO), and the United Kingdom Space Agency. A complete and detailed list is available on the *Euclid* website (www.euclid-ec.org). This work has made use of the *Euclid* Quick Release Q1 data from the *Euclid* mission of the European Space Agency (ESA), 2025, https://doi.org/10.57780/esa-2853f3b. This work has made use of CosmoHub, developed by PIC (maintained by IFAE and CIEMAT) in collaboration with ICE-CSIC. CosmoHub received funding from the Spanish government (MCIN/AEI/10.13039/501100011033), the EU NextGeneration/PRTR (PRTR-C17.I1), and the Generalitat de Catalunya. Based on data from UNIONS, a scientific collaboration using three Hawaii-based telescopes: CFHT, Pan-STARRS, and Subaru www.skysurvey.cc. Based on data from the Dark Energy Camera (DECam) on the Blanco 4-m Telescope at CTIO in Chile https://www.darkenergysurvey.org

References

Agertz, O., & Kravtsov, A. V. 2016, ApJ, 824, 79
Ahumada, R., Allende Prieto, C., Almeida, A., et al. 2020, ApJS, 249, 3
Allen, P. D., Driver, S. P., Graham, A. W., et al. 2006, MNRAS, 371, 2
Arango-Toro, R. C., Ilbert, O., Ciesla, L., et al. 2025, A&A, 696, A159
Athanassoula, E., Rodionov, S. A., Peschken, N., & Lambert, J. C. 2016, ApJ, 821, 90
Baldry, I. K., Balogh, M. L., Bower, R. G., et al. 2006, MNRAS, 373, 469
Bekki, K., & Couch, W. J. 2011, MNRAS, 415, 1783
Bell, E. F., Wolf, C., Meisenheimer, K., et al. 2004, ApJ, 608, 752
Bertin, E., Schefer, M., Apostolakos, N., et al. 2020, ASP Conf. Ser., 527, 461
Birnboim, Y., & Dekel, A. 2003, MNRAS, 345, 349
Blake, C., Amon, A., Childress, M., et al. 2016, MNRAS, 462, 4240
Bongiorno, A., Schulze, A., Merloni, A., et al. 2016, A&A, 588, A78
Boselli, A., Fossati, M., & Sun, M. 2022, A&ARv, 30, 3
Bouché, N., Dekel, A., Genzel, R., et al. 2010, ApJ, 718, 1001
Bournaud, F. 2016, Astrophys. Space Sci. Lib., 418, 355
Bower, R. G., Benson, A. J., Malbon, R., et al. 2006, MNRAS, 370, 645
Brammer, G. B., Sánchez-Janssen, R., Labbé, I., et al. 2012, ApJ, 758, L17
Bremer, M. N., Phillipps, S., Kelvin, L. S., et al. 2018, MNRAS, 476, 12
Brinchmann, J., Charlot, S., White, S. D. M., et al. 2004, MNRAS, 351, 1151
Carretero, J., Tallada, P., Casals, J., et al. 2017, Proceedings of the European Physical Society Conference on High Energy Physics, 5–12 July, 488
Casey, C. M., Kartaltepe, J. S., Drakos, N. E., et al. 2023, ApJ, 954, 31
Chabrier, G. 2003, PASP, 115, 763
Chauke, P., van der Wel, A., Pacifici, C., et al. 2019, ApJ, 877, 48
Chen, Z., Faber, S. M., Koo, D. C., et al. 2020, ApJ, 897, 102
Chiang, Y.-K., Overzier, R. A., Gebhardt, K., & Henriques, B. 2017, ApJ, 844, L23
Childress, M. J., Lidman, C., Davis, T. M., et al. 2017, MNRAS, 472, 273
Ciotti, L., D'Ercole, A., Pellegrini, S., & Renzini, A. 1991, ApJ, 376, 380

Coil, A. L., Blanton, M. R., Burles, S. M., et al. 2011, ApJ, 741, 8
Colless, M., Dalton, G., Maddox, S., et al. 2001, MNRAS, 328, 1039
Correa, C. A., Schaye, J., & Trayford, J. W. 2019, MNRAS, 484, 4401
Cox, T. J., Jonsson, P., Somerville, R. S., Primack, J. R., & Dekel, A. 2008, MNRAS, 384, 386
Crain, R. A., Schaye, J., Bower, R. G., et al. 2015, MNRAS, 450, 1937
Croton, D. J., Springel, V., White, S. D. M., et al. 2006, MNRAS, 365, 11
Daddi, E., Delvecchio, I., Dimauro, P., et al. 2022, A&A, 661, L7
Dark Energy Survey Collaboration (Abbott, T., et al.) 2016, MNRAS, 460, 1270
Davies, L. J. M., Thorne, J. E., Bellstedt, S., et al. 2025, MNRAS, 540, 1870
Dekel, A., Sari, R., & Ceverino, D. 2009a, ApJ, 703, 785
Dekel, A., Birnboim, Y., Engel, G., et al. 2009b, Nature, 457, 451
Dekel, A., Sarkar, K. C., Birnboim, Y., Mandelker, N., & Li, Z. 2023, MNRAS, 523, 3201
DESI Collaboration (Aghamousa, A., et al.) 2016, ArXiv e-prints [arXiv:1611.00036]
DESI Collaboration (Adame, A. G., et al.) 2024, AJ, 168, 58
D'Eugenio, F., Cameron, A. J., Scholtz, J., et al. 2025, ApJS, 277, 4
Dressler, A. 1980, ApJ, 236, 351
Dressler, A., Oemler, A., Couch, W. J., et al. 1997, ApJ, 490, 577
Dubois, Y., Peirani, S., Pichon, C., et al. 2016, MNRAS, 463, 3948
Elbaz, D., Dickinson, M., Hwang, H. S., et al. 2011, A&A, 533, A119
Euclid Collaboration (Desprez, G., et al.) 2020, A&A, 644, A31
Euclid Collaboration (Moneti, A., et al.) 2022, A&A, 658, A126
Euclid Collaboration (Scaramella, R., et al.) 2022, A&A, 662, A112
Euclid Collaboration (Enia, A., et al.) 2024, A&A, 691, A175
Euclid Collaboration (Castander, F., et al.) 2025, A&A, 697, A5
Euclid Collaboration (Cleland, C., et al.) 2025, A&A, submitted [arXiv:2503.15313] (Euclid Q1 SI)
Euclid Collaboration (Cropper, M., et al.) 2025, A&A, 697, A2
Euclid Collaboration (Jahnke, K., et al.) 2025, A&A, 697, A3
Euclid Collaboration (McPartland, C. J. R., et al.) 2025, A&A, 695, A259
Euclid Collaboration (Mellier, Y., et al.) 2025, A&A, 697, A1
Euclid Quick Release Q1 2025, https://doi.org/10.57780/esa-2853f3b
Euclid Collaboration (Aussel, H., et al.) 2026, A&A, 711, A1 (Euclid Q1 SI)
Euclid Collaboration (Bisigello, L., et al.) 2026, A&A, 711, A24 (Euclid Q1 SI)
Euclid Collaboration (Copin, Y., et al.) 2026, A&A, 711, A6 (Euclid Q1 SI)
Euclid Collaboration (Enia, A., et al.) 2026, A&A, 711, A14 (Euclid Q1 SI)
Euclid Collaboration (Gillard, W., et al.) 2026, A&A, 711, A227 (Euclid Q1 SI)
Euclid Collaboration (Laigle, C., et al.) 2026, A&A, 711, A36 (Euclid Q1 SI)
Euclid Collaboration (Le Brun, V., et al.) 2026, A&A, 711, A7 (Euclid Q1 SI)
Euclid Collaboration (Matamoro Zatarain, T., et al.) 2026, A&A, 711, A20 (Euclid Q1 SI)
Euclid Collaboration (McCracken, H. J., et al.) 2026, A&A, 711, A2 (Euclid Q1 SI)
Euclid Collaboration (Polenta, G., et al.) 2026, A&A, 711, A3 (Euclid Q1 SI)
Euclid Collaboration (Quilley, L., et al.) 2026, A&A, 711, A8 (Euclid Q1 SI)
Euclid Collaboration (Romelli, E., et al.) 2026, A&A, 711, A4 (Euclid Q1 SI)
Euclid Collaboration (Tucci, M., et al.) 2026, A&A, 711, A5 (Euclid Q1 SI)
Feldmann, R., Carollo, C. M., Mayer, L., et al. 2010, ApJ, 709, 218
Ferrarese, L., & Merritt, D. 2000, ApJ, 539, L9
Flaugher, B., Diehl, H. T., Honscheid, K., et al. 2015, AJ, 150, 150
Foltz, R., Wilson, G., Muzzin, A., et al. 2018, ApJ, 866, 136
Fossati, M., Wilman, D. J., Mendel, J. T., et al. 2017, ApJ, 835, 153
Gunn, J. E., & Gott, J. R., III 1972, ApJ, 176, 1
Gwyn, S., McConnachie, A. W., Cuillandre, J.-C., et al. 2025, AJ, 170, 324
Häring, N., & Rix, H.-W. 2004, ApJ, 604, L89
Hopkins, P. F., Hernquist, L., Cox, T. J., & Kereš, D. 2008, ApJS, 175, 356
Hubble, E. P. 1926, ApJ, 64, 321
Huchra, J. P., Macri, L. M., Masters, K. L., et al. 2012, ApJS, 199, 26
Huertas-Company, M., Iyer, K. G., Angeloudi, E., et al. 2024, A&A, 685, A48
Huertas-Company, M., Shuntov, M., Dong, Y., et al. 2025, A&A, 704, A94
Ilbert, O., Salvato, M., Le Floc'h, E., et al. 2010, ApJ, 709, 644
Jones, D. H., Read, M. A., Saunders, W., et al. 2009, MNRAS, 399, 683
Kauffmann, G., Heckman, T. M., White, S. D. M., et al. 2003, MNRAS, 341, 54
Kereš, D., Katz, N., Weinberg, D. H., & Davé, R. 2005, MNRAS, 363, 2
Kreckel, K., Platen, E., Aragón-Calvo, M. A., et al. 2012, AJ, 144, 16
Kriek, M., Shapley, A. E., Reddy, N. A., et al. 2015, ApJS, 218, 15
Kümmel, M., Álvarez-Ayllón, A., Bertin, E., et al. 2022, ArXiv e-prints [arXiv:2212.02428]
Lang, P., Wuyts, S., Somerville, R. S., et al. 2014, ApJ, 788, 11
Larson, R. B., Tinsley, B. M., & Caldwell, C. N. 1980, ApJ, 237, 692
Laureijs, R., Amiaux, J., Arduini, S., et al. 2011, arXiv eprints [arXiv:1110.3193]
Le Fèvre, O., Vettolani, G., Garilli, B., et al. 2005, A&A, 439, 845
Lidman, C., Tucker, B. E., Davis, T. M., et al. 2020, MNRAS, 496, 19
Liu, C., Hao, L., Wang, H., & Yang, X. 2019, ApJ, 878, 69
Lupton, R., Blanton, M. R., Fekete, G., et al. 2004, PASP, 116, 133
Lyu, Y., Magnelli, B., Elbaz, D., et al. 2025, A&A, 693, A313
Malavasi, N., Pozzetti, L., Cucciati, O., Bardelli, S., & Cimatti, A. 2016, A&A, 585, A116
Man, A., & Belli, S. 2018, Nat. Astron., 2, 695
Mancini, C., Daddi, E., Juneau, S., et al. 2019, MNRAS, 489, 1265
Martig, M., Bournaud, F., Teyssier, R., & Dekel, A. 2009, ApJ, 707, 250
Martín-Navarro, I., Shankar, F., & Mezcua, M. 2022, MNRAS, 513, L10
Masters, K. L., Mosleh, M., Romer, A. K., et al. 2010, MNRAS, 405, 783
McCracken, H. J., Wolk, M., Colombi, S., et al. 2015, MNRAS, 449, 901
McIntosh, D. H., Wagner, C., Cooper, A., et al. 2014, MNRAS, 442, 533
Merritt, D. 1983, ApJ, 264, 24
Noguchi, M. 1999, ApJ, 514, 77
Oke, J. B., & Gunn, J. E. 1983, ApJ, 266, 713
Pan, R., Suess, K. A., Marchesini, D., et al. 2025, ApJ, 990, L24
Peng, Y.-J., Lilly, S. J., Kovač, K., et al. 2010, ApJ, 721, 193
Peng, Y.-J., Lilly, S. J., Renzini, A., & Carollo, M. 2012, ApJ, 757, 4
Pentericci, L., McLure, R. J., Franzetti, P., Garilli, B., & the VANDELS team 2018, ArXiv e-prints [arXiv:1811.05298]
Perez, J., Valenzuela, O., Tissera, P. B., & Michel-Dansac, L. 2013, MNRAS, 436, 259
Phillipps, S., Bremer, M. N., Hopkins, A. M., et al. 2019, MNRAS, 485, 5559
Planck Collaboration VI. 2020, A&A, 641, A6
Popesso, P., Concas, A., Morselli, L., et al. 2019, MNRAS, 483, 3213
Popesso, P., Concas, A., Cresci, G., et al. 2023, MNRAS, 519, 1526
Postman, M., Franx, M., Cross, N. J. G., et al. 2005, ApJ, 623, 721
Pozzetti, L., Bolzonella, M., Zucca, E., et al. 2010, A&A, 523, A13
Quilley, L., & de Lapparent, V. 2022, A&A, 666, A170
Read, J. I., Wilkinson, M. I., Evans, N. W., Gilmore, G., & Kleyna, J. T. 2006, MNRAS, 366, 429
Rodriguez-Gomez, V., Sales, L. V., Genel, S., et al. 2017, MNRAS, 467, 3083
Sachdeva, S., Saha, K., & Singh, H. P. 2017, ApJ, 840, 79
Sales, L. V., Navarro, J. F., Theuns, T., et al. 2012, MNRAS, 423, 1544
Salim, S., & Narayanan, D. 2020, ARA&A, 58, 529
Schawinski, K., Urry, C. M., Simmons, B. D., et al. 2014, MNRAS, 440, 889
Schaye, J., Crain, R. A., Bower, R. G., et al. 2015, MNRAS, 446, 521
Schreiber, C., Pannella, M., Elbaz, D., et al. 2015, A&A, 575, A74
Scoville, N., Aussel, H., Brusa, M., et al. 2007, ApJS, 172, 1
Sérsic, J. L. 1963, Boletin de la Asociacion Argentina de Astronomia La Plata Argentina, 6, 41
Strateva, I., Ivezić, Ž., Knapp, G. R., et al. 2001, AJ, 122, 1861
Tacchella, S., Diemer, B., Hernquist, L., et al. 2019, MNRAS, 487, 5416
Talia, M., Schreiber, C., Garilli, B., et al. 2023, A&A, 678, A25
Tallada, P., Carretero, J., Casals, J., et al. 2020, Astron. Comput., 32, 100391
Tan, Q.-H., Daddi, E., Magnelli, B., et al. 2024, Nature, 636, 69
Übler, H., Naab, T., Oser, L., et al. 2014, MNRAS, 443, 2092
van den Bosch, F. C., Aquino, D., Yang, X., et al. 2008, MNRAS, 387, 79
Watson, W. A., Iliev, I. T., D'Aloisio, A., et al. 2013, MNRAS, 433, 1230
Wuyts, S., Förster Schreiber, N. M., van der Wel, A., et al. 2011, ApJ, 742, 96
Xu, K., Wang, T., Daddi, E., et al. 2025, ArXiv e-prints [arXiv:2503.21724]
Yang, H., Liao, S., Fattahi, A., et al. 2024, MNRAS, 535, 1394
Yu, S.-Y., Kalinova, V., Colombo, D., et al. 2022, A&A, 666, A175
Yuan, F., Lidman, C., Davis, T. M., et al. 2015, MNRAS, 452, 3047

[1] CEA Saclay, DFR/IRFU, Service d'Astrophysique, Bât. 709, 91191 Gif-sur-Yvette, France
[2] INAF-Osservatorio di Astrofisica e Scienza dello Spazio di Bologna, Via Piero Gobetti 93/3, 40129 Bologna, Italy
[3] Université Paris-Saclay, Université Paris Cité, CEA, CNRS, AIM, 91191 Gif-sur-Yvette, France
[4] Dipartimento di Fisica e Astronomia, Università di Bologna, Via Gobetti 93/2, 40129 Bologna, Italy
[5] Kapteyn Astronomical Institute, University of Groningen, PO Box 800, 9700 AV Groningen, The Netherlands
[6] Université Paris Cité, CNRS, Astroparticule et Cosmologie, 75013 Paris, France
[7] INAF-Osservatorio Astronomico di Trieste, Via G. B. Tiepolo 11, 34143 Trieste, Italy
[8] Institute de Physique du Globe de Paris, 1 Rue Jussieu, 75005 Paris, France
[9] Dipartimento di Fisica "G. Occhialini", Università degli Studi di Milano Bicocca, Piazza della Scienza 3, 20126 Milano, Italy
[10] INAF-Osservatorio Astronomico di Brera, Via Brera 28, 20122 Milano, Italy
[11] Instituto de Astrofísica e Ciências do Espaço, Universidade do Porto, CAUP, Rua das Estrelas, PT4150-762 Porto, Portugal

[12] Departamento de Física e Astronomia, Faculdade de Ciências, Universidade do Porto, Rua do Campo Alegre 687, PT4169-007 Porto, Portugal
[13] INAF-Istituto di Astrofisica e Planetologia Spaziali, Via del Fosso del Cavaliere, 100, 00100 Roma, Italy
[14] Institut d'Astrophysique de Paris, UMR 7095, CNRS, and Sorbonne Université, 98 bis Boulevard Arago, 75014 Paris, France
[15] Institut d'Astrophysique de Paris, 98 bis Boulevard Arago, 75014 Paris, France
[16] Centre de Recherche Astrophysique de Lyon, UMR5574, CNRS, Université Claude Bernard Lyon 1, ENS de Lyon, 69230 Saint-Genis-Laval, France
[17] Univ. Lille, CNRS, Centrale Lille, UMR 9189 CRIStAL, 59000 Lille, France
[18] Université Paris-Saclay, CNRS, Institut d'Astrophysique Spatiale, 91405 Orsay, France
[19] Department of Physics, Oxford University, Keble Road, Oxford OX1 3RH, UK
[20] Dipartimento di Fisica e Astronomia "Augusto Righi" – Alma Mater Studiorum Università di Bologna, Via Piero Gobetti 93/2, 40129 Bologna, Italy
[21] School of Physics & Astronomy, University of Southampton, Highfield Campus, Southampton SO17 1BJ, UK
[22] Sterrenkundig Observatorium, Universiteit Gent, Krijgslaan 281 S9, 9000 Gent, Belgium
[23] Center for Astronomy and Astrophysics and Department of Physics, Fudan University, Shanghai 200438, PR China
[24] Dipartimento di Fisica – Sezione di Astronomia, Università di Trieste, Via Tiepolo 11, 34131 Trieste, Italy
[25] Institute of Science and Technology Austria (ISTA), Am Campus 1, 3400 Klosterneuburg, Austria
[26] Department of Astronomy, University of Geneva, Ch. d'Ecogia 16, 1290 Versoix, Switzerland
[27] Cosmic Dawn Center (DAWN)
[28] Niels Bohr Institute, University of Copenhagen, Jagtvej 128, 2200 Copenhagen, Denmark
[29] Leiden Observatory, Leiden University, Einsteinweg 55, 2333 CC Leiden, The Netherlands
[30] Department of Physics and Astronomy, University of British Columbia, Vancouver, BC V6T 1Z1, Canada
[31] ESAC/ESA, Camino Bajo del Castillo, s/n, Urb. Villafranca del Castillo, 28692 Villanueva de la Cañada, Madrid, Spain
[32] School of Mathematics and Physics, University of Surrey, Guildford, Surrey GU2 7XH, UK
[33] IFPU, Institute for Fundamental Physics of the Universe, Via Beirut 2, 34151 Trieste, Italy
[34] INFN, Sezione di Trieste, Via Valerio 2, 34127 Trieste, TS, Italy
[35] SISSA, International School for Advanced Studies, Via Bonomea 265, 34136 Trieste, TS, Italy
[36] INFN-Sezione di Bologna, Viale Berti Pichat 6/2, 40127 Bologna, Italy
[37] INAF-Osservatorio Astronomico di Padova, Via dell'Osservatorio 5, 35122 Padova, Italy
[38] Max Planck Institute for Extraterrestrial Physics, Giessenbachstr. 1, 85748 Garching, Germany
[39] Universitäts-Sternwarte München, Fakultät für Physik, Ludwig-Maximilians-Universität München, Scheinerstrasse 1, 81679 München, Germany
[40] Dipartimento di Fisica, Università di Genova, Via Dodecaneso 33, 16146 Genova, Italy
[41] INFN-Sezione di Genova, Via Dodecaneso 33, 16146 Genova, Italy
[42] Department of Physics "E. Pancini", University Federico II, Via Cinthia 6, 80126 Napoli, Italy
[43] INAF-Osservatorio Astronomico di Capodimonte, Via Moiariello 16, 80131 Napoli, Italy
[44] Faculdade de Ciências da Universidade do Porto, Rua do Campo de Alegre, 4150-007 Porto, Portugal
[45] European Southern Observatory, Karl-Schwarzschild-Str. 2, 85748 Garching, Germany
[46] Dipartimento di Fisica, Università degli Studi di Torino, Via P. Giuria 1, 10125 Torino, Italy
[47] INFN-Sezione di Torino, Via P. Giuria 1, 10125 Torino, Italy
[48] INAF-Osservatorio Astrofisico di Torino, Via Osservatorio 20, 10025 Pino Torinese, (TO), Italy
[49] European Space Agency/ESTEC, Keplerlaan 1, 2201 AZ Noordwijk, The Netherlands
[50] INAF-IASF Milano, Via Alfonso Corti 12, 20133 Milano, Italy
[51] Centro de Investigaciones Energéticas, Medioambientales y Tecnológicas (CIEMAT), Avenida Complutense 40, 28040 Madrid, Spain
[52] Port d'Informació Científica, Campus UAB, C. Albareda s/n, 08193 Bellaterra, (Barcelona), Spain
[53] Institute for Theoretical Particle Physics and Cosmology (TTK), RWTH Aachen University, 52056 Aachen, Germany
[54] Deutsches Zentrum für Luft- und Raumfahrt e. V. (DLR), Linder Höhe, 51147 Köln, Germany
[55] INAF-Osservatorio Astronomico di Roma, Via Frascati 33, 00078 Monteporzio Catone, Italy
[56] INFN section of Naples, Via Cinthia 6, 80126, Napoli, Italy
[57] Institute for Astronomy, University of Hawaii, 2680 Woodlawn Drive, Honolulu, HI 96822, USA
[58] Dipartimento di Fisica e Astronomia "Augusto Righi" – Alma Mater Studiorum Università di Bologna, Viale Berti Pichat 6/2, 40127 Bologna, Italy
[59] Instituto de Astrofísica de Canarias, Vía Láctea, 38205 La Laguna, Tenerife, Spain
[60] Institute for Astronomy, University of Edinburgh, Royal Observatory, Blackford Hill, Edinburgh EH9 3HJ, UK
[61] European Space Agency/ESRIN, Largo Galileo Galilei 1, 00044 Frascati, Roma, Italy
[62] Université Claude Bernard Lyon 1, CNRS/IN2P3, IP2I Lyon, UMR 5822, Villeurbanne F-69100, France
[63] Institut de Ciències del Cosmos (ICCUB), Universitat de Barcelona (IEEC-UB), Martí i Franquès 1, 08028 Barcelona, Spain
[64] Institució Catalana de Recerca i Estudis Avançats (ICREA), Passeig de Lluís Companys 23, 08010 Barcelona, Spain
[65] UCB Lyon 1, CNRS/IN2P3, IUF, IP2I Lyon, 4 Rue Enrico Fermi, 69622 Villeurbanne, France
[66] Mullard Space Science Laboratory, University College London, Holmbury St Mary, Dorking, Surrey RH5 6NT, UK
[67] Departamento de Física, Faculdade de Ciências, Universidade de Lisboa, Edifício C8, Campo Grande, PT1749-016 Lisboa, Portugal
[68] Instituto de Astrofísica e Ciências do Espaço, Faculdade de Ciências, Universidade de Lisboa, Campo Grande, 1749-016 Lisboa, Portugal
[69] INFN-Padova, Via Marzolo 8, 35131 Padova, Italy
[70] Aix-Marseille Université, CNRS/IN2P3, CPPM, Marseille, France
[71] INFN-Bologna, Via Irnerio 46, 40126 Bologna, Italy
[72] University Observatory, LMU Faculty of Physics, Scheinerstrasse 1, 81679 Munich, Germany
[73] Herzberg Astronomy and Astrophysics Research Centre, 5071 W. Saanich Rd., Victoria, BC V9E 2E7, Canada
[74] Institute of Theoretical Astrophysics, University of Oslo, P.O. Box 1029, Blindern 0315, Oslo, Norway
[75] Jet Propulsion Laboratory, California Institute of Technology, 4800 Oak Grove Drive, Pasadena, CA 91109, USA
[76] Department of Physics, Lancaster University, Lancaster LA1 4YB, UK
[77] Felix Hormuth Engineering, Goethestr. 17, 69181 Leimen, Germany
[78] Technical University of Denmark, Elektrovej 327, 2800 Kgs. Lyngby, Denmark
[79] Cosmic Dawn Center (DAWN), Denmark
[80] Max-Planck-Institut für Astronomie, Königstuhl 17, 69117 Heidelberg, Germany
[81] NASA Goddard Space Flight Center, Greenbelt, MD 20771, USA
[82] Department of Physics and Astronomy, University College London, Gower Street, London WC1E 6BT, UK

[83] Department of Physics and Helsinki Institute of Physics, Gustaf Hällströmin katu 2, University of Helsinki, 00014 Helsinki, Finland
[84] Université de Genève, Département de Physique Théorique and Centre for Astroparticle Physics, 24 quai Ernest-Ansermet, CH-1211 Genève 4, Switzerland
[85] Department of Physics, P.O. Box 64, University of Helsinki, 00014 Helsinki, Finland
[86] Helsinki Institute of Physics, Gustaf Hällströmin katu 2, University of Helsinki, 00014 Helsinki, Finland
[87] Laboratoire d'etude de l'Univers et des phenomenes eXtremes, Observatoire de Paris, Université PSL, Sorbonne Université, CNRS, 92190 Meudon, France
[88] SKAO, Jodrell Bank, Lower Withington, Macclesfield SK11 9FT, UK
[89] Centre de Calcul de l'IN2P3/CNRS, 21 Avenue Pierre de Coubertin, 69627 Villeurbanne Cedex, France
[90] Dipartimento di Fisica "Aldo Pontremoli", Università degli Studi di Milano, Via Celoria 16, 20133 Milano, Italy
[91] INFN-Sezione di Milano, Via Celoria 16, 20133 Milano, Italy
[92] Universität Bonn, Argelander-Institut für Astronomie, Auf dem Hügel 71, 53121 Bonn, Germany
[93] INFN-Sezione di Roma, Piazzale Aldo Moro, 2 – c/o Dipartimento di Fisica, Edificio G. Marconi, 00185 Roma, Italy
[94] Aix-Marseille Université, CNRS, CNES, LAM, Marseille, France
[95] Department of Physics, Institute for Computational Cosmology, Durham University, South Road, Durham DH1 3LE, UK
[96] CNRS-UCB International Research Laboratory, Centre Pierre Binétruy, IRL2007, CPB-IN2P3, Berkeley, USA
[97] University of Applied Sciences and Arts of Northwestern Switzerland, School of Engineering, 5210 Windisch, Switzerland
[98] Institute of Physics, Laboratory of Astrophysics, Ecole Polytechnique Fédérale de Lausanne (EPFL), Observatoire de Sauverny, 1290 Versoix, Switzerland
[99] Telespazio UK S.L. for European Space Agency (ESA), Camino bajo del Castillo, s/n, Urbanizacion Villafranca del Castillo, Villanueva de la Cañada 28692, Madrid, Spain
[100] Institut de Física d'Altes Energies (IFAE), The Barcelona Institute of Science and Technology, Campus UAB, 08193 Bellaterra, (Barcelona), Spain
[101] DARK, Niels Bohr Institute, University of Copenhagen, Jagtvej 155, 2200 Copenhagen, Denmark
[102] Waterloo Centre for Astrophysics, University of Waterloo, Waterloo, Ontario N2L 3G1, Canada
[103] Department of Physics and Astronomy, University of Waterloo, Waterloo, Ontario N2L 3G1, Canada
[104] Perimeter Institute for Theoretical Physics, Waterloo, Ontario N2L 2Y5, Canada
[105] Space Science Data Center, Italian Space Agency, Via del Politecnico snc, 00133 Roma, Italy
[106] Centre National d'Etudes Spatiales – Centre Spatial de Toulouse, 18 Avenue Edouard Belin, 31401 Toulouse Cedex 9, France
[107] Institute of Space Science, Str. Atomistilor, Nr. 409 Măgurele, Ilfov 077125, Romania
[108] Dipartimento di Fisica e Astronomia "G. Galilei", Università di Padova, Via Marzolo 8, 35131 Padova, Italy
[109] Institut für Theoretische Physik, University of Heidelberg, Philosophenweg 16, 69120 Heidelberg, Germany
[110] Institut de Recherche en Astrophysique et Planétologie (IRAP), Université de Toulouse, CNRS, UPS, CNES, 14 Av. Edouard Belin, 31400 Toulouse, France
[111] Université St Joseph; Faculty of Sciences, Beirut, Lebanon
[112] Departamento de Física, FCFM, Universidad de Chile, Blanco Encalada, 2008 Santiago, Chile
[113] Universität Innsbruck, Institut für Astro- und Teilchenphysik, Technikerstr. 25/8, 6020 Innsbruck, Austria
[114] Institut d'Estudis Espacials de Catalunya (IEEC), Edifici RDIT, Campus UPC, 08860 Castelldefels, Barcelona, Spain
[115] Satlantis, University Science Park, Sede Bld 48940, Leioa-Bilbao, Spain
[116] Institute of Space Sciences (ICE, CSIC), Campus UAB, Carrer de Can Magrans, s/n, 08193 Barcelona, Spain
[117] Centre for Electronic Imaging, Open University, Walton Hall, Milton Keynes MK7 6AA, UK
[118] Infrared Processing and Analysis Center, California Institute of Technology, Pasadena, CA 91125, USA
[119] Instituto de Astrofísica e Ciências do Espaço, Faculdade de Ciências, Universidade de Lisboa, Tapada da Ajuda, 1349-018 Lisboa, Portugal
[120] Universidad Politécnica de Cartagena, Departamento de Electrónica y Tecnología de Computadoras, Plaza del Hospital 1, 30202 Cartagena, Spain
[121] Astronomisches Rechen-Institut, Zentrum für Astronomie der Universität Heidelberg, Mönchhofstr. 12-14, 69120 Heidelberg, Germany
[122] Dipartimento di Fisica e Scienze della Terra, Università degli Studi di Ferrara, Via Giuseppe Saragat 1, 44122 Ferrara, Italy
[123] Istituto Nazionale di Fisica Nucleare, Sezione di Ferrara, Via Giuseppe Saragat 1, 44122 Ferrara, Italy
[124] INAF, Istituto di Radioastronomia, Via Piero Gobetti 101, 40129 Bologna, Italy
[125] Astronomical Observatory of the Autonomous Region of the Aosta Valley (OAVdA), Loc. Lignan 39, I-11020 Nus (Aosta Valley), Italy
[126] Université Côte d'Azur, Observatoire de la Côte d'Azur, CNRS, Laboratoire Lagrange, Bd de l'Observatoire, CS 34229, 06304 Nice Cedex 4, France
[127] Instituto de Astrofísica de Canarias (IAC); Departamento de Astrofísica, Universidad de La Laguna (ULL), 38200 La Laguna, Tenerife, Spain
[128] Université PSL, Observatoire de Paris, Sorbonne Université, CNRS, LERMA, 75014 Paris, France
[129] Université Paris-Cité, 5 Rue Thomas Mann, 75013 Paris, France
[130] Aurora Technology for European Space Agency (ESA), Camino bajo del Castillo, s/n, Urbanizacion Villafranca del Castillo, Villanueva de la Cañada 28692, Madrid, Spain
[131] ICL, Junia, Université Catholique de Lille, LITL, 59000 Lille, France
[132] ICSC – Centro Nazionale di Ricerca in High Performance Computing, Big Data e Quantum Computing, Via Magnanelli 2, Bologna, Italy
[133] Instituto de Física Teórica UAM-CSIC, Campus de Cantoblanco, 28049 Madrid, Spain
[134] CERCA/ISO, Department of Physics, Case Western Reserve University, 10900 Euclid Avenue, Cleveland, OH 44106, USA
[135] Technical University of Munich, TUM School of Natural Sciences, Physics Department, James-Franck-Str. 1, 85748 Garching, Germany
[136] Max-Planck-Institut für Astrophysik, Karl-Schwarzschild-Str. 1, 85748 Garching, Germany
[137] Laboratoire Univers et Théorie, Observatoire de Paris, Université PSL, Université Paris Cité, CNRS, 92190 Meudon, France
[138] Departamento de Física Fundamental, Universidad de Salamanca, Plaza de la Merced s/n, 37008 Salamanca, Spain
[139] Université de Strasbourg, CNRS, Observatoire Astronomique de Strasbourg, UMR 7550, 67000 Strasbourg, France
[140] Center for Data-Driven Discovery, Kavli IPMU (WPI), UTIAS, The University of Tokyo, Kashiwa, Chiba 277-8583, Japan
[141] Ludwig-Maximilians-University, Schellingstrasse 4, 80799 Munich, Germany
[142] Max-Planck-Institut für Physik, Boltzmannstr. 8, 85748 Garching, Germany
[143] Jodrell Bank Centre for Astrophysics, Department of Physics and Astronomy, University of Manchester, Oxford Road, Manchester M13 9PL, UK
[144] California Institute of Technology, 1200 E California Blvd, Pasadena, CA 91125, USA
[145] Department of Physics & Astronomy, University of California Irvine, Irvine, CA 92697, USA

[146] Departamento Física Aplicada, Universidad Politécnica de Cartagena, Campus Muralla del Mar, 30202 Cartagena, Murcia, Spain
[147] Instituto de Física de Cantabria, Edificio Juan Jordá, Avenida de los Castros, 39005 Santander, Spain
[148] Observatorio Nacional, Rua General Jose Cristino, 77-Bairro Imperial de Sao Cristovao, Rio de Janeiro 20921-400, Brazil
[149] INFN, Sezione di Lecce, Via per Arnesano, CP-193, 73100 Lecce, Italy
[150] Department of Mathematics and Physics E. De Giorgi, University of Salento, Via per Arnesano, CP-I93, 73100 Lecce, Italy
[151] INAF-Sezione di Lecce, c/o Dipartimento Matematica e Fisica, Via per Arnesano, 73100 Lecce, Italy
[152] Institute of Cosmology and Gravitation, University of Portsmouth, Portsmouth PO1 3FX, UK
[153] Department of Astronomy, University of Florida, Bryant Space Science Center, Gainesville, FL 32611, USA
[154] Department of Computer Science, Aalto University, PO Box 15400, Espoo FI-00 076, Finland
[155] Instituto de Astrofísica de Canarias, c/ Via Lactea s/n, La Laguna 38200, Spain
[156] Departamento de Astrofísica de la Universidad de La Laguna, Avda. Francisco Sanchez, La Laguna 38200, Spain
[157] Caltech/IPAC, 1200 E. California Blvd., Pasadena, CA 91125, USA
[158] Ruhr University Bochum, Faculty of Physics and Astronomy, Astronomical Institute (AIRUB), German Centre for Cosmological Lensing (GCCL), 44780 Bochum, Germany
[159] Department of Physics and Astronomy, Vesilinnantie 5, University of Turku, 20014 Turku, Finland
[160] Serco for European Space Agency (ESA), Camino bajo del Castillo, s/n, Urbanizacion Villafranca del Castillo, Villanueva de la Cañada 28692, Madrid, Spain
[161] ARC Centre of Excellence for Dark Matter Particle Physics, Melbourne, Australia
[162] Centre for Astrophysics & Supercomputing, Swinburne University of Technology, Hawthorn, Victoria 3122, Australia
[163] Department of Physics and Astronomy, University of the Western Cape, Bellville, Cape Town 7535, South Africa
[164] DAMTP, Centre for Mathematical Sciences, Wilberforce Road, Cambridge CB3 0WA, UK
[165] Kavli Institute for Cosmology Cambridge, Madingley Road, Cambridge CB3 0HA, UK
[166] Department of Astrophysics, University of Zurich, Winterthurerstrasse 190, 8057 Zurich, Switzerland
[167] Department of Physics, Centre for Extragalactic Astronomy, Durham University, South Road, Durham DH1 3LE, UK
[168] IRFU, CEA, Université Paris-Saclay, 91191 Gif-sur-Yvette Cedex, France
[169] Oskar Klein Centre for Cosmoparticle Physics, Department of Physics, Stockholm University, Stockholm SE-106 91, Sweden
[170] Astrophysics Group, Blackett Laboratory, Imperial College London, London SW7 2AZ, UK
[171] Univ. Grenoble Alpes, CNRS, Grenoble INP, LPSC-IN2P3, 53, Avenue des Martyrs, 38000 Grenoble, France
[172] INAF-Osservatorio Astrofisico di Arcetri, Largo E. Fermi 5, 50125 Firenze, Italy
[173] Dipartimento di Fisica, Sapienza Università di Roma, Piazzale Aldo Moro 2, 00185 Roma, Italy
[174] Centro de Astrofísica da Universidade do Porto, Rua das Estrelas, 4150-762 Porto, Portugal
[175] HE Space for European Space Agency (ESA), Camino bajo del Castillo, s/n, Urbanizacion Villafranca del Castillo, Villanueva de la Cañada 28692, Madrid, Spain
[176] INAF – Osservatorio Astronomico d'Abruzzo, Via Maggini, 64100 Teramo, Italy
[177] Theoretical astrophysics, Department of Physics and Astronomy, Uppsala University, Box 516, 751 37 Uppsala, Sweden
[178] Minnesota Institute for Astrophysics, University of Minnesota, 116 Church St SE, Minneapolis, MN 55455, USA
[179] Mathematical Institute, University of Leiden, Einsteinweg 55, 2333 CA Leiden, The Netherlands
[180] Institute of Astronomy, University of Cambridge, Madingley Road, Cambridge CB3 0HA, UK
[181] Department of Physics and Astronomy, University of California, Davis, CA 95616, USA
[182] Department of Astrophysical Sciences, Peyton Hall, Princeton University, Princeton, NJ 08544, USA
[183] Space physics and astronomy research unit, University of Oulu, Pentti Kaiteran katu 1, FI-90014 Oulu, Finland
[184] Center for Computational Astrophysics, Flatiron Institute, 162 5th Avenue, 10010 New York, NY, USA

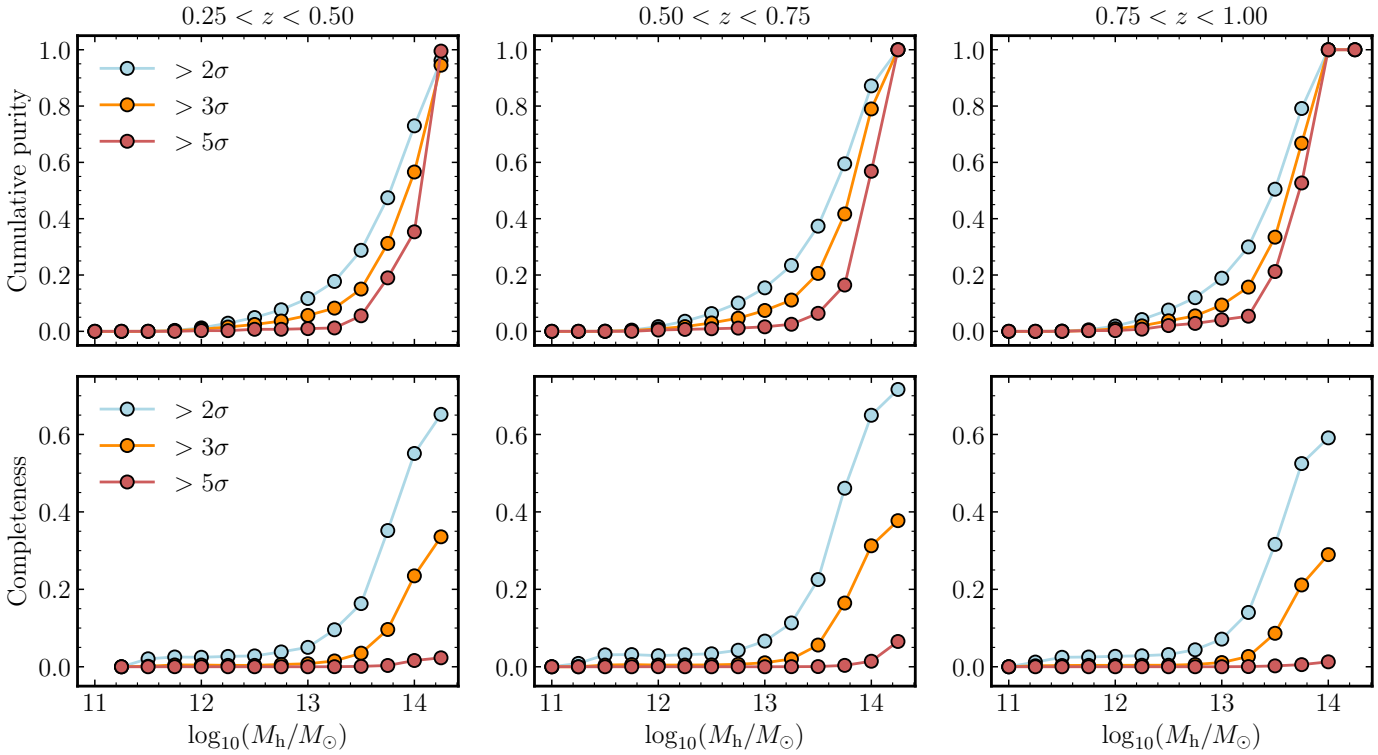


Fig. A.1. Cumulative purity and completeness of our estimation of the density field as a function of the halo mass and of the threshold employed to define over-dense regions, as assessed from the Euclid `Flagship-2` simulation. A description of the two quantities can be found in Appendix A.

Appendix A: Properties of the density field

In order to estimate the reliability of our reconstruction of the density field in the EDFs, we apply the same pipeline described in Sect. 3 to the simulated data from the `Flagship-2` simulation (see Sect. 4.4). We adopt a quantitative approach by introducing two different metrics. The first is the cumulative purity (upper row of Fig. A.1): for a given value of the halo mass ($M_{\rm h}^*$), we define this quantity as the number of central galaxies with $M_{\rm h} < M_{\rm h}^*$ and with a density contrast $\log_{10}(1+\delta)$ above $n\sigma$ from the median divided by the total amount of central galaxies with $\log_{10}(1+\delta)$ above the same threshold. This quantity tells us what percentage of low-mass halos are included in our selection. From Fig. A.1, we can see how for all thresholds, more than 80% of sources that – according to our selection – belong to over-densities actually have an halo mass compatible with a group ($M_{\rm h} > 10^{13}\,M_\odot$).

The second metric that we employ is called completeness (lower row of Fig. A.1) and is defined, for a given value of the halo mass ($M_{\rm h}^*$), as the fraction of central galaxies with $M_{\rm h} = M_{\rm h}^*$ and with a density contrast above $n\sigma$ from the median, divided by the total amount of central galaxies with $M_{\rm h} = M_{\rm h}^*$. In other words, this quantity tells us what fraction of central galaxies with a given halo mass is recovered by our selection and – therefore – how complete is our sample of over-densities. From Fig. A.1, we can see how our selection is able to identify more than half of the massive structures ($M > 10^{14}\,M_\odot$) when a threshold of 2σ is adopted, but how this fraction rapidly decreases when we choose a higher threshold or when we go to lower halo masses.

In summary, our selection of high-density regions is definitely pure (i.e. only structures with massive halos are retrieved by our selection), but not totally complete (several massive structure are missed by our selection). This result is easily explained by the employment of photometric redshift and, therefore, of thick redshift slices. This produces a shot noise due to the galaxies in the line-of-sight diluting the signal of real over-densities and biasing our selection towards the most massive structures.